

Study of $e^+e^- \rightarrow p\bar{p}$ via initial-state radiation at *BABAR*

J. P. Lees, V. Poireau, and V. Tisserand

*Laboratoire d'Annecy-le-Vieux de Physique des Particules (LAPP),
Université de Savoie, CNRS/IN2P3, F-74941 Annecy-Le-Vieux, France*

E. Grauges

Universitat de Barcelona, Facultat de Física, Departament ECM, E-08028 Barcelona, Spain

A. Palano^{ab}

INFN Sezione di Bari^a; Dipartimento di Fisica, Università di Bari^b, I-70126 Bari, Italy

G. Eigen and B. Stugu

University of Bergen, Institute of Physics, N-5007 Bergen, Norway

D. N. Brown, L. T. Kerth, Yu. G. Kolomensky, and G. Lynch

Lawrence Berkeley National Laboratory and University of California, Berkeley, California 94720, USA

H. Koch and T. Schroeder

Ruhr Universität Bochum, Institut für Experimentalphysik 1, D-44780 Bochum, Germany

D. J. Asgeirsson, C. Hearty, T. S. Mattison, J. A. McKenna, and R. Y. So

University of British Columbia, Vancouver, British Columbia, Canada V6T 1Z1

A. Khan

Brunel University, Uxbridge, Middlesex UB8 3PH, United Kingdom

V. E. Blinov, A. R. Buzykaev, V. P. Druzhinin, V. B. Golubev, E. A. Kravchenko, A. P. Onuchin,

S. I. Serednyakov, Yu. I. Skovpen, E. P. Solodov, K. Yu. Todyshev, and A. N. Yushkov

Budker Institute of Nuclear Physics SB RAS, Novosibirsk 630090, Russia

D. Kirkby, A. J. Lankford, and M. Mandelkern

University of California at Irvine, Irvine, California 92697, USA

B. Dey, J. W. Gary, O. Long, and G. M. Vitug

University of California at Riverside, Riverside, California 92521, USA

C. Campagnari, M. Franco Sevilla, T. M. Hong, D. Kovalskyi, J. D. Richman, and C. A. West

University of California at Santa Barbara, Santa Barbara, California 93106, USA

A. M. Eisner, W. S. Lockman, A. J. Martinez, B. A. Schumm, and A. Seiden

University of California at Santa Cruz, Institute for Particle Physics, Santa Cruz, California 95064, USA

D. S. Chao, C. H. Cheng, B. Echenard, K. T. Flood, D. G. Hitlin, P. Ongmongkolkul, F. C. Porter, and A. Y. Rakitin

California Institute of Technology, Pasadena, California 91125, USA

R. Andreassen, Z. Huard, B. T. Meadows, M. D. Sokoloff, and L. Sun

University of Cincinnati, Cincinnati, Ohio 45221, USA

P. C. Bloom, W. T. Ford, A. Gaz, U. Nauenberg, J. G. Smith, and S. R. Wagner

University of Colorado, Boulder, Colorado 80309, USA

R. Ayad* and W. H. Toki

Colorado State University, Fort Collins, Colorado 80523, USA

B. Spaan

Technische Universität Dortmund, Fakultät Physik, D-44221 Dortmund, Germany

K. R. Schubert and R. Schwierz

Technische Universität Dresden, Institut für Kern- und Teilchenphysik, D-01062 Dresden, Germany

D. Bernard and M. Verderi

Laboratoire Leprince-Ringuet, Ecole Polytechnique, CNRS/IN2P3, F-91128 Palaiseau, France

P. J. Clark and S. Playfer

University of Edinburgh, Edinburgh EH9 3JZ, United Kingdom

D. Bettoni^a, C. Bozzi^a, R. Calabrese^{ab}, G. Cibinetto^{ab}, E. Fioravanti^{ab},

I. Garzia^{ab}, E. Luppi^{ab}, L. Piemontese^a, and V. Santoro^a

INFN Sezione di Ferrara^a; Dipartimento di Fisica, Università di Ferrara^b, I-44100 Ferrara, Italy

R. Baldini-Ferrolì, A. Calcaterra, R. de Sangro, G. Finocchiaro,

P. Patteri, I. M. Peruzzi,[†] M. Piccolo, M. Rama, and A. Zallo

INFN Laboratori Nazionali di Frascati, I-00044 Frascati, Italy

R. Contri^{ab}, E. Guido^{ab}, M. Lo Vetere^{ab}, M. R. Monge^{ab}, S. Passaggio^a, C. Patrignani^{ab}, and E. Robutti^a

INFN Sezione di Genova^a; Dipartimento di Fisica, Università di Genova^b, I-16146 Genova, Italy

B. Bhuyan and V. Prasad

Indian Institute of Technology Guwahati, Guwahati, Assam, 781 039, India

M. Morii

Harvard University, Cambridge, Massachusetts 02138, USA

A. Adametz and U. Uwer

Universität Heidelberg, Physikalisches Institut, Philosophenweg 12, D-69120 Heidelberg, Germany

H. M. Lacker and T. Lueck

Humboldt-Universität zu Berlin, Institut für Physik, Newtonstr. 15, D-12489 Berlin, Germany

P. D. Dauncey

Imperial College London, London, SW7 2AZ, United Kingdom

U. Mallik

University of Iowa, Iowa City, Iowa 52242, USA

C. Chen, J. Cochran, W. T. Meyer, S. Prell, and A. E. Rubin

Iowa State University, Ames, Iowa 50011-3160, USA

A. V. Gritsan

Johns Hopkins University, Baltimore, Maryland 21218, USA

N. Arnaud, M. Davier, D. Derkach, G. Grosdidier, F. Le Diberder, A. M. Lutz,

B. Malaescu, P. Roudeau, M. H. Schune, A. Stocchi, and G. Wormser

*Laboratoire de l'Accélérateur Linéaire, IN2P3/CNRS et Université Paris-Sud 11,
Centre Scientifique d'Orsay, B. P. 34, F-91898 Orsay Cedex, France*

D. J. Lange and D. M. Wright

Lawrence Livermore National Laboratory, Livermore, California 94550, USA

J. P. Coleman, J. R. Fry, E. Gabathuler, D. E. Hutchcroft, D. J. Payne, and C. Touramanis

University of Liverpool, Liverpool L69 7ZE, United Kingdom

A. J. Bevan, F. Di Lodovico, R. Sacco, and M. Sigamani
Queen Mary, University of London, London, E1 4NS, United Kingdom

G. Cowan
University of London, Royal Holloway and Bedford New College, Egham, Surrey TW20 0EX, United Kingdom

D. N. Brown and C. L. Davis
University of Louisville, Louisville, Kentucky 40292, USA

A. G. Denig, M. Fritsch, W. Gradl, K. Griessinger, A. Hafner, and E. Prencipe
Johannes Gutenberg-Universität Mainz, Institut für Kernphysik, D-55099 Mainz, Germany

R. J. Barlow[‡] and G. D. Lafferty
University of Manchester, Manchester M13 9PL, United Kingdom

E. Behn, R. Cenci, B. Hamilton, A. Jawahery, and D. A. Roberts
University of Maryland, College Park, Maryland 20742, USA

C. Dallapiccola
University of Massachusetts, Amherst, Massachusetts 01003, USA

R. Cowan, D. Dujmic, and G. Sciolla
Massachusetts Institute of Technology, Laboratory for Nuclear Science, Cambridge, Massachusetts 02139, USA

R. Cheaib, P. M. Patel,[§] and S. H. Robertson
McGill University, Montréal, Québec, Canada H3A 2T8

P. Biassoni^{ab}, N. Neri^a, and F. Palombo^{ab}
INFN Sezione di Milano^a; Dipartimento di Fisica, Università di Milano^b, I-20133 Milano, Italy

L. Cremaldi, R. Godang,[¶] R. Kroeger, P. Sonnek, and D. J. Summers
University of Mississippi, University, Mississippi 38677, USA

X. Nguyen, M. Simard, and P. Taras
Université de Montréal, Physique des Particules, Montréal, Québec, Canada H3C 3J7

G. De Nardo^{ab}, D. Monorchio^{ab}, G. Onorato^{ab}, and C. Sciacca^{ab}
*INFN Sezione di Napoli^a; Dipartimento di Scienze Fisiche,
 Università di Napoli Federico II^b, I-80126 Napoli, Italy*

M. Martinelli and G. Raven
NIKHEF, National Institute for Nuclear Physics and High Energy Physics, NL-1009 DB Amsterdam, The Netherlands

C. P. Jessop and J. M. LoSecco
University of Notre Dame, Notre Dame, Indiana 46556, USA

K. Honscheid and R. Kass
Ohio State University, Columbus, Ohio 43210, USA

J. Brau, R. Frey, N. B. Sinev, D. Strom, and E. Torrence
University of Oregon, Eugene, Oregon 97403, USA

E. Feltresi^{ab}, N. Gagliardi^{ab}, M. Margoni^{ab}, M. Morandin^a,
 M. Posocco^a, M. Rotondo^a, G. Simi^a, F. Simonetto^{ab}, and R. Stroili^{ab}
INFN Sezione di Padova^a; Dipartimento di Fisica, Università di Padova^b, I-35131 Padova, Italy

S. Akar, E. Ben-Haim, M. Bomben, G. R. Bonneaud, H. Briand, G. Calderini,
 J. Chauveau, O. Hamon, Ph. Leruste, G. Marchiori, J. Ocariz, and S. Sitt

*Laboratoire de Physique Nucléaire et de Hautes Energies,
IN2P3/CNRS, Université Pierre et Marie Curie-Paris6,
Université Denis Diderot-Paris7, F-75252 Paris, France*

M. Biasini^{ab}, E. Manoni^{ab}, S. Pacetti^{ab}, and A. Rossi^{ab}
INFN Sezione di Perugia^a; Dipartimento di Fisica, Università di Perugia^b, I-06100 Perugia, Italy

C. Angelini^{ab}, G. Batignani^{ab}, S. Bettarini^{ab}, M. Carpinelli^{ab},** G. Casarosa^{ab}, A. Cervelli^{ab}, F. Forti^{ab},
M. A. Giorgi^{ab}, A. Lusiani^{ac}, B. Oberhof^{ab}, E. Paoloni^{ab}, A. Perez^a, G. Rizzo^{ab}, and J. J. Walsh^a
INFN Sezione di Pisa^a; Dipartimento di Fisica, Università di Pisa^b; Scuola Normale Superiore di Pisa^c, I-56127 Pisa, Italy

D. Lopes Pegna, J. Olsen, and A. J. S. Smith
Princeton University, Princeton, New Jersey 08544, USA

F. Anulli^a, R. Faccini^{ab}, F. Ferrarotto^a, F. Ferroni^{ab}, M. Gaspero^{ab}, L. Li Gioi^a, M. A. Mazzoni^a, and G. Piredda^a
*INFN Sezione di Roma^a; Dipartimento di Fisica,
Università di Roma La Sapienza^b, I-00185 Roma, Italy*

C. Büniger, O. Grünberg, T. Hartmann, T. Leddig, C. Voß, and R. Waldi
Universität Rostock, D-18051 Rostock, Germany

T. Adye, E. O. Olaiya, and F. F. Wilson
Rutherford Appleton Laboratory, Chilton, Didcot, Oxon, OX11 0QX, United Kingdom

S. Emery, G. Hamel de Monchenault, G. Vasseur, and Ch. Yèche
CEA, Irfu, SPP, Centre de Saclay, F-91191 Gif-sur-Yvette, France

D. Aston, D. J. Bard, J. F. Benitez, C. Cartaro, M. R. Convery, J. Dorfan, G. P. Dubois-Felsmann,
W. Dunwoodie, M. Ebert, R. C. Field, B. G. Fulsom, A. M. Gabareen, M. T. Graham, C. Hast, W. R. Innes,
M. H. Kelsey, P. Kim, M. L. Kocian, D. W. G. S. Leith, P. Lewis, D. Lindemann, B. Lindquist, S. Luitz,
V. Luth, H. L. Lynch, D. B. MacFarlane, D. R. Muller, H. Neal, S. Nelson, M. Perl, T. Pulliam,
B. N. Ratcliff, A. Roodman, A. A. Salnikov, R. H. Schindler, A. Snyder, D. Su, M. K. Sullivan, J. Va'vra,
A. P. Wagner, W. F. Wang, W. J. Wisniewski, M. Wittgen, D. H. Wright, H. W. Wulsin, and V. Ziegler
SLAC National Accelerator Laboratory, Stanford, California 94309 USA

W. Park, M. V. Purohit, R. M. White, and J. R. Wilson
University of South Carolina, Columbia, South Carolina 29208, USA

A. Randle-Conde and S. J. Sekula
Southern Methodist University, Dallas, Texas 75275, USA

M. Bellis, P. R. Burchat, T. S. Miyashita, and E. M. T. Puccio
Stanford University, Stanford, California 94305-4060, USA

M. S. Alam and J. A. Ernst
State University of New York, Albany, New York 12222, USA

R. Gorodeisky, N. Guttman, D. R. Peimer, and A. Soffer
Tel Aviv University, School of Physics and Astronomy, Tel Aviv, 69978, Israel

S. M. Spanier
University of Tennessee, Knoxville, Tennessee 37996, USA

J. L. Ritchie, A. M. Ruland, R. F. Schwitters, and B. C. Wray
University of Texas at Austin, Austin, Texas 78712, USA

J. M. Izen and X. C. Lou
University of Texas at Dallas, Richardson, Texas 75083, USA

F. Bianchi^{ab}, D. Gamba^{ab}, and S. Zambito^{ab}
INFN Sezione di Torino^a; Dipartimento di Fisica Sperimentale, Università di Torino^b, I-10125 Torino, Italy

L. Lanceri^{ab} and L. Vitale^{ab}
INFN Sezione di Trieste^a; Dipartimento di Fisica, Università di Trieste^b, I-34127 Trieste, Italy

F. Martinez-Vidal, A. Oyanguren, and P. Villanueva-Perez
IFIC, Universitat de Valencia-CSIC, E-46071 Valencia, Spain

H. Ahmed, J. Albert, Sw. Banerjee, F. U. Bernlochner, H. H. F. Choi, G. J. King,
 R. Kowalewski, M. J. Lewczuk, I. M. Nugent, J. M. Roney, R. J. Sobie, and N. Tasneem
University of Victoria, Victoria, British Columbia, Canada V8W 3P6

T. J. Gershon, P. F. Harrison, and T. E. Latham
Department of Physics, University of Warwick, Coventry CV4 7AL, United Kingdom

H. R. Band, S. Dasu, Y. Pan, R. Prepost, and S. L. Wu
University of Wisconsin, Madison, Wisconsin 53706, USA

The process $e^+e^- \rightarrow p\bar{p}\gamma$ is studied using 469 fb⁻¹ of integrated luminosity collected with the BABAR detector at the PEP-II collider, at an e^+e^- center-of-mass energy of 10.6 GeV. From the analysis of the $p\bar{p}$ invariant mass spectrum, the energy dependence of the cross section for $e^+e^- \rightarrow p\bar{p}$ is measured from threshold to 4.5 GeV. The energy dependence of the ratio of electric and magnetic form factors, $|G_E/G_M|$, and the asymmetry in the proton angular distribution are measured for $p\bar{p}$ masses below 3 GeV. We also measure the branching fractions for the decays $J/\psi \rightarrow p\bar{p}$ and $\psi(2S) \rightarrow p\bar{p}$.

PACS numbers: 13.66.Bc, 14.20.Dh, 13.40.Gp, 13.25.Gv

I. INTRODUCTION

In this paper we use the initial-state-radiation (ISR) technique to study the $e^+e^- \rightarrow p\bar{p}$ process in a wide range of center-of-mass (c.m.) energies. The Born cross section for the ISR process $e^+e^- \rightarrow p\bar{p}\gamma$ (Fig. 1), integrated over the nucleon momenta, is given by

$$\frac{d^2\sigma_{e^+e^- \rightarrow p\bar{p}\gamma}(M_{p\bar{p}})}{dM_{p\bar{p}} d\cos\theta_\gamma^*} = \frac{2M_{p\bar{p}}}{s} W(s, x, \theta_\gamma^*) \sigma_{p\bar{p}}(M_{p\bar{p}}), \quad (1)$$

where $\sigma_{p\bar{p}}(m)$ is the Born cross section for the nonradiative process $e^+e^- \rightarrow p\bar{p}$, $M_{p\bar{p}}$ is the $p\bar{p}$ invariant mass, \sqrt{s} is the nominal e^+e^- c.m. energy, $x \equiv 2E_\gamma^*/\sqrt{s} = 1 - M_{p\bar{p}}^2/s$, and E_γ^* and θ_γ^* are the ISR photon energy and polar angle, respectively, in the e^+e^- c.m. frame.¹

The function [1]

$$W(s, x, \theta_\gamma^*) = \frac{\alpha}{\pi x} \left(\frac{2 - 2x + x^2}{\sin^2\theta_\gamma^*} - \frac{x^2}{2} \right) \quad (2)$$

is the probability of ISR photon emission for $\theta_\gamma^* \gg m_e/\sqrt{s}$, where α is the fine-structure constant and m_e is the electron mass. The cross section for the $e^+e^- \rightarrow p\bar{p}$ process is given by

$$\sigma_{p\bar{p}}(M_{p\bar{p}}) = \frac{4\pi\alpha^2\beta C}{3M_{p\bar{p}}^2} \left[|G_M(M_{p\bar{p}})|^2 + \frac{2m_p^2}{M_{p\bar{p}}^2} |G_E(M_{p\bar{p}})|^2 \right], \quad (3)$$

where m_p is the nominal proton mass, $\beta = \sqrt{1 - 4m_p^2/M_{p\bar{p}}^2}$, and C is the Coulomb correction factor (see, for example, Ref. [2] and references therein), which makes the cross section nonzero at threshold ($C = y/(1 - e^{-y})$ with $y = \pi\alpha/\beta$). The cross section depends on the magnetic form factor (G_M) and the electric form factor (G_E); at threshold, $|G_E| = |G_M|$. From the measurement of the cross section a linear combination of the squared form factors can be determined. We define the effective form factor

$$|F_p(M_{p\bar{p}})| = \sqrt{\frac{|G_M(M_{p\bar{p}})|^2 + 2m_p^2/M_{p\bar{p}}^2 |G_E(M_{p\bar{p}})|^2}{1 + 2m_p^2/M_{p\bar{p}}^2}}, \quad (4)$$

which is proportional to the square root of the measured $e^+e^- \rightarrow p\bar{p}$ cross section.

*Now at the University of Tabuk, Tabuk 71491, Saudi Arabia

†Also with Università di Perugia, Dipartimento di Fisica, Perugia, Italy

‡Now at the University of Huddersfield, Huddersfield HD1 3DH, UK

§Deceased

¶Now at University of South Alabama, Mobile, Alabama 36688, USA

**Also with Università di Sassari, Sassari, Italy

¹ Throughout this paper, the asterisk denotes quantities in the e^+e^- center-of-mass frame. All other variables except θ_p are defined in the laboratory frame.

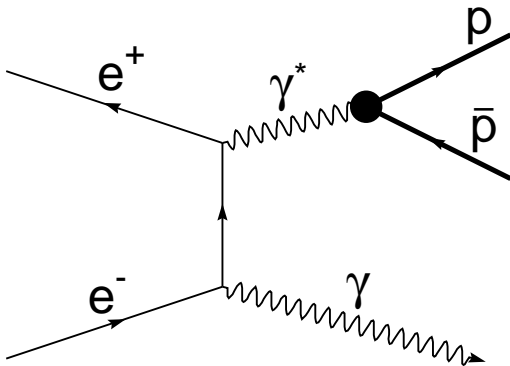


FIG. 1: The Feynman diagram for the signal ISR process $e^+e^- \rightarrow p\bar{p}\gamma$.

The modulus of the ratio of the electric and magnetic form factors can be determined from the distribution of θ_p , the angle between the proton momentum in the $p\bar{p}$ rest frame and the momentum of the $p\bar{p}$ system in the e^+e^- c.m. frame. This distribution can be expressed as a sum of terms proportional to $|G_M|^2$ and $|G_E|^2$. The full differential cross section for $e^+e^- \rightarrow p\bar{p}\gamma$ can be found, for example, in Ref. [3]. The θ_p dependences of the G_E and G_M terms are close to $\sin^2\theta_p$ and $1 + \cos^2\theta_p$, respectively.

Direct measurements of the $e^+e^- \rightarrow p\bar{p}$ cross section have been performed in e^+e^- experiments [4–10]. Most of these measurements have an accuracy of (20–30)%. The cross section and the proton form factor were deduced assuming $|G_E| = |G_M|$, and the measured proton angular distributions [5, 6, 10] did not contradict this assumption. More precise measurements of the proton form factor have been performed in $p\bar{p} \rightarrow e^+e^-$ experiments [11–13]. In the PS170 experiment [11] at LEAR, the proton form factor was measured from threshold ($p\bar{p}$ annihilation at rest) up to a c.m. energy 2.05 GeV. The ratio $|G_E/G_M|$ was measured with about 30% accuracy and was found to be compatible with unity. The LEAR data show a strong dependence of the form factor on c.m. energy near threshold, and very little dependence in the range 1.95–2.05 GeV. Analyses from Fermilab experiments E760 [12] and E835 [13] show a strong decrease of the form factor at c.m. energies higher than 3 GeV, in agreement with perturbative QCD, which predicts that the dependence should be $\alpha_s^2(m^2)/m^4$. However, the recent precision e^+e^- measurement [10] based on CLEO data indicates that the decrease of the form factor at energies about 4 GeV is somewhat slower.

The previous *BABAR* study [14] of the process $e^+e^- \rightarrow p\bar{p}$ using the ISR technique was based on about half of the data that were finally collected in the experiment. The $e^+e^- \rightarrow p\bar{p}$ cross section was measured for c.m. energies up to 4.5 GeV. This measurement yielded a significant improvement in precision for energies below 3 GeV.

In contrast to previous e^+e^- and $p\bar{p}$ experiments, the *BABAR* measurement did not assume that $|G_E| = |G_M|$. The ISR approach provides full θ_p coverage, and hence high sensitivity to $|G_E/G_M|$. The energy dependence of the form-factor ratio $|G_E/G_M|$ was measured for c.m. energies below 3 GeV. For energies up to 2.1 GeV, this ratio was found to be significantly greater than unity, in disagreement with the PS170 measurement [11].

In this work we update the analysis of Ref. [14] using the full *BABAR* data sample collected at and near the $\Upsilon(4S)$ resonance.

II. THE *BABAR* DETECTOR AND DATA SAMPLES

We analyse a data sample corresponding to an integrated luminosity of 469 fb^{-1} recorded with the *BABAR* detector [15] at the SLAC PEP-II asymmetric-energy collider. At PEP-II, 9-GeV electrons collide with 3.1-GeV positrons at a c.m. energy of 10.58 GeV (the $\Upsilon(4S)$ mass). About 10% of the data are collected at 10.54 GeV.

Charged-particle tracking is provided by a five-layer silicon vertex tracker (SVT) and a 40-layer drift chamber (DCH), operating in a 1.5-T axial magnetic field. The transverse momentum resolution is 0.47% at 1 GeV/c. The position and energy of a photon-produced cluster are measured with a CsI(Tl) electromagnetic calorimeter, which yields an energy resolution of 3% at 1 GeV. Charged-particle identification is provided by specific ionization (dE/dx) measurements in the SVT and DCH, and by an internally reflecting ring-imaging Cherenkov detector (DIRC). Muons are identified in the solenoid's instrumented flux return (IFR), which consists of iron plates interleaved with either resistive plate chambers or streamer tubes [16].

Signal and background ISR processes are simulated with Monte Carlo (MC) event generators based on Ref. [17]. The differential cross section for $e^+e^- \rightarrow p\bar{p}\gamma$ is taken from Ref. [3]. To analyze the experimental proton angular distribution, two samples of signal events are generated, one with $G_E = 0$ and the other with $G_M = 0$. Since the polar-angle distribution of the ISR photon is peaked near 0° and 180° , the MC events are generated with a restriction on the photon polar angle: $20^\circ < \theta_\gamma^* < 160^\circ$ (the corresponding angular range in the laboratory frame is $12^\circ < \theta_\gamma < 146^\circ$). Extra soft-photon radiation from the initial state is generated by the structure function method [18]. To restrict the maximum energy of the extra photons, the invariant mass of the hadron system and the ISR photon is required to be greater than $8 \text{ GeV}/c^2$. For background $e^+e^- \rightarrow \mu^+\mu^-\gamma$, $\pi^+\pi^-\gamma$, and $K^+K^-\gamma$ processes, final-state bremsstrahlung is generated using the PHOTOS package [19]. Background from $e^+e^- \rightarrow q\bar{q}$ is simulated with the JETSET [20] event generator; JETSET also generates ISR events with hadron invariant mass above $2 \text{ GeV}/c^2$, and therefore can be used to study ISR back-

ground with baryons in the final state. The dominant background process, $e^+e^- \rightarrow p\bar{p}\pi^0$, is simulated separately by generating the angular and energy distributions for the final-state hadrons according to three-body phase space.

The response of the *BABAR* detector is simulated using the Geant4 [21] package. The simulation takes into account the variations in the detector and beam background conditions over the running period of the experiment.

III. EVENT SELECTION

The preliminary selection of $e^+e^- \rightarrow p\bar{p}\gamma$ candidates requires that all of the final-state particles be detected inside a fiducial volume. Since a significant fraction of the events contains beam-generated spurious tracks and photon candidates, we select events with at least two tracks with opposite charge and at least one photon candidate with $E_\gamma^* > 3$ GeV. The polar angle of the photon is required to be in the well-understood region of the calorimeter: $20^\circ < \theta_\gamma < 137.5^\circ$. Each charged-particle track must originate from the interaction region, have transverse momentum greater than 0.1 GeV/c and be in the angular region $25.8^\circ < \theta < 137.5^\circ$. The latter requirement is needed to provide particle identification (PID) from the DIRC. To suppress background from radiative Bhabha events, we reject events for which the ratios of calorimetric energy deposition to momentum for the two highest-momentum tracks satisfy the condition $(E_{\text{cal},1}/p_1 - 1)^2 + (E_{\text{cal},2}/p_2 - 1)^2 < 0.35^2$.

For events passing the preliminary selection, a kinematic fit is performed to the $e^+e^- \rightarrow h^+h^-\gamma$ hypothesis with requirements of total energy and momentum conservation. Here h can be e , μ , π , K or p , and γ is the photon candidate with the highest energy in the e^+e^- c.m. frame. For events with more than two charged tracks, the fit uses the two oppositely charged tracks that pass closest to the interaction point. The MC simulation does not accurately reproduce the shape of the photon energy resolution function. This leads to a difference in the distributions of the χ^2 of the kinematic fit for data and simulated events. To reduce this difference, only the measured direction of the ISR photon is used in the fit; its energy is a free fit parameter. For each of the five mass hypotheses, the corrected angles and energies of the particles and the χ^2 value are obtained from the fit.

The expected number of events from the background processes $e^+e^- \rightarrow \pi^+\pi^-\gamma$, $\mu^+\mu^-\gamma$, and $K^+K^-\gamma$ exceeds the number of signal events by two to three orders of magnitude. To suppress these backgrounds, we require that both charged particles be identified as protons according to the specific ionization (dE/dx) measured in the SVT and DCH, and the Cherenkov angle measured in the DIRC. This requirement suppresses pion and muon backgrounds by a factor of 3×10^4 , and kaon background by a factor 10^4 , with a loss of approximately 30% of the

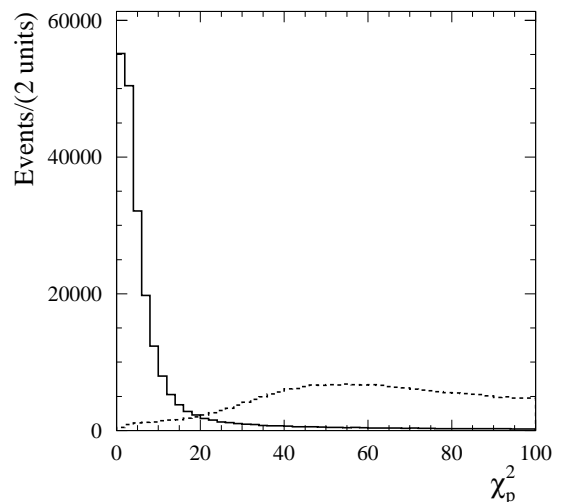


FIG. 2: The χ_p^2 distribution for simulated $e^+e^- \rightarrow p\bar{p}\gamma$ (solid histogram) and $e^+e^- \rightarrow K^+K^-\gamma$ (dashed histogram, arbitrary normalization) events.

signal events.

Background is further suppressed through requirements on the χ^2 of the kinematic fit: $\chi_p^2 < 30$ and $\chi_K^2 > 30$, where χ_p^2 and χ_K^2 are the χ^2 values of the kinematic fit for the proton and kaon mass hypotheses, respectively. The χ_p^2 distribution for simulated $p\bar{p}\gamma$ events is shown in Fig. 2. The long tail at high χ^2 is due to events with extra soft photons emitted in the initial state. The dashed histogram is the χ_p^2 distribution for $K^+K^-\gamma$ simulated events. The χ^2 requirements lead to the loss of 25% of the signal events, but provide additional background suppression by a factor of 50 for pion and muon events, and a factor of 30 for kaon events.

The $p\bar{p}$ invariant mass distribution is shown in Fig. 3 for the 8298 data events that satisfy the selection criteria. Most of the events have invariant mass below 3 GeV/c². Signals from $J/\psi \rightarrow p\bar{p}$ and $\psi(2S) \rightarrow p\bar{p}$ decays are clearly seen.

IV. BACKGROUND SUBTRACTION

Potential sources of background in the sample of selected $e^+e^- \rightarrow p\bar{p}\gamma$ candidates are the processes $e^+e^- \rightarrow \pi^+\pi^-\gamma$, $e^+e^- \rightarrow K^+K^-\gamma$, $e^+e^- \rightarrow \mu^+\mu^-\gamma$, and $e^+e^- \rightarrow e^+e^-\gamma$ in which the charged particles are misidentified as protons. Background contributions from processes with protons and neutral particle(s) in the final state, such as $e^+e^- \rightarrow p\bar{p}\pi^0$, $p\bar{p}\eta$, $p\bar{p}\pi^0\gamma$, etc., are also anticipated.

Of particular interest is the possible background from the process $e^+e^- \rightarrow p\bar{p}\gamma$ with the photon emitted from the final state. Due to the different charge-conjugation parity of the amplitudes corresponding to initial-state radiation and final-state radiation (FSR), their interference

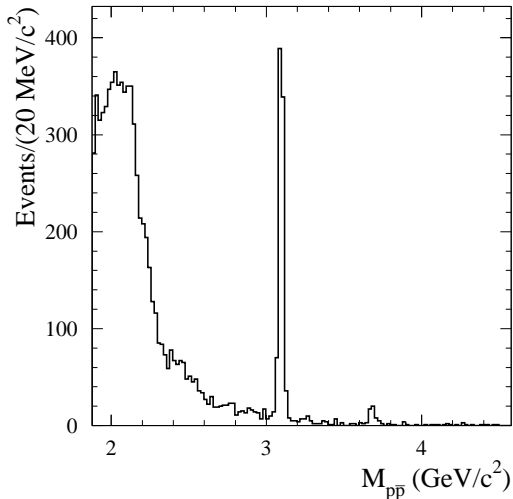


FIG. 3: The $p\bar{p}$ invariant mass spectrum for the selected data $p\bar{p}\gamma$ candidates. The left edge of the plot corresponds to the $p\bar{p}$ threshold.

does not contribute to the total $e^+e^- \rightarrow p\bar{p}\gamma$ cross section. The contribution of the FSR amplitude is estimated to be [22] $d\sigma/dm \approx |F_{\text{ax}}|^2 8m\alpha^3\beta/(27s^2)$, where F_{ax} is the axial proton form factor. Assuming $|F_{\text{ax}}| \approx |G_M|$, the ratio of the FSR and ISR cross sections is estimated to be about 10^{-3} for $p\bar{p}$ invariant masses below $4.5 \text{ GeV}/c^2$. We conclude that the FSR background is small and so may be neglected.

A. Background contributions from $e^+e^- \rightarrow \pi^+\pi^-\gamma$, $e^+e^- \rightarrow K^+K^-\gamma$, $e^+e^- \rightarrow \mu^+\mu^-\gamma$ and $e^+e^- \rightarrow e^+e^-\gamma$

To estimate the background contribution from $e^+e^- \rightarrow \pi^+\pi^-\gamma$, data and simulated $\pi^+\pi^-\gamma$ events are selected with the following requirements on PID and on the χ^2 of the kinematic fit:

1. one proton candidate, $\chi_\pi^2 < 20$;
2. one proton candidate, $\chi_p^2 < 30$, $\chi_K^2 > 30$;
3. two proton candidates, $\chi_\pi^2 < 20$;
4. two proton candidates, $\chi_p^2 < 30$, $\chi_K^2 > 30$.

Here χ_π^2 is the χ^2 of the kinematic fit for the pion mass hypothesis. The fourth set of conditions corresponds to the standard selection criteria for $p\bar{p}\gamma$ candidates.

The invariant mass $M_{\pi\pi}$ of the two charged particles under the pion-mass hypothesis is calculated; the $M_{\pi\pi}$ distributions for data selected with criteria 2 and 3 are shown in Fig. 4. The data spectra are fit with a sum of the mass spectra for simulated $\pi^+\pi^-\gamma$ events (ρ -meson line shape with ω - ρ interference) and a linear background

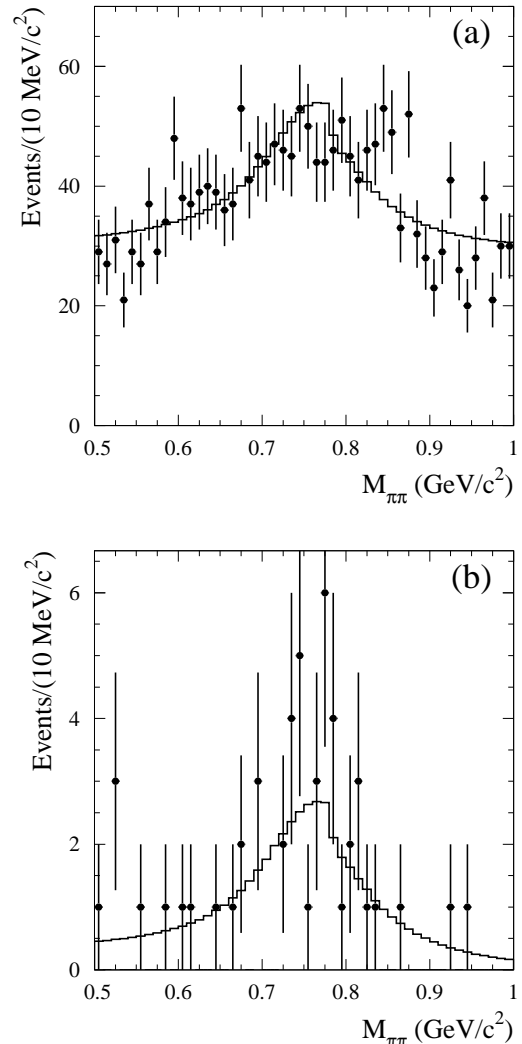


FIG. 4: (a) The $M_{\pi\pi}$ spectrum for data events with $\chi_p^2 < 30$ and $\chi_K^2 > 30$, and one proton candidate (selection 2 in the text); (b) the same spectrum for data events with $\chi_\pi^2 < 20$ and two proton candidates (selection 3 in the text). The histograms are the results of the fit described in the text.

term. The numbers of $\pi\pi\gamma$ events with $0.5 < M_{\pi\pi} < 1 \text{ GeV}/c^2$ obtained from the fits for selections 1–3 are listed in Table I, together with the corresponding numbers from the $\pi^+\pi^-\gamma$ MC simulation. The spectrum for selection 4 is fit by a linear function; no ρ -meson contribution is needed to describe this spectrum.

Since the simulation correctly predicts the numbers of pion events for selections 1–3, it can be used to estimate the pion background for the standard selection 4. We observe no events satisfying the standard selection criteria in the $\pi\pi\gamma$ MC sample. The corresponding upper limit on $\pi\pi\gamma$ background in the data sample is 5.2 events at 90% confidence level (CL). The estimated pion background is less than 0.1% of the number of selected $p\bar{p}\gamma$ candidates.

TABLE I: The numbers of $\pi\pi\gamma$ events for data and MC simulation with $0.5 < M_{\pi\pi} < 1$ GeV/ c^2 that satisfy different selection criteria for data and MC simulation. The data numbers are obtained from the fits to the $M_{\pi\pi}$ distributions described in the text.

selection	data	MC
1	15310 ± 160	14800 ± 180
2	400 ± 60	460 ± 30
3	41 ± 8	48 ± 11

Similarly, the number of $e^+e^- \rightarrow K^+K^-\gamma$ events can be estimated from the number of events in the ϕ meson peak in the distribution of invariant mass of the charged particles calculated under the kaon hypothesis. It is found that the $K^+K^-\gamma$ MC simulation predicts reasonably well the numbers of kaon events in the data sample with one identified kaon and the standard χ^2 conditions, and in the data sample with two identified kaons and $\chi_K^2 < 20$. Therefore we use the MC simulation to estimate kaon background for the standard selection. The estimated background, 1.6 ± 0.8 events, is significantly less than 0.1% of the number of data events selected.

The kinematic properties of the $e^+e^- \rightarrow e^+e^-\gamma$ process are used to estimate the electron background. About 50% of $e^+e^-\gamma$ events have e^+e^- invariant mass between 3 and 7 GeV/ c^2 and $\cos\psi^* < -0.98$, where ψ^* is the angle between the two tracks in the initial e^+e^- c.m. frame. In the event sample with two proton candidates we do not find events having the above characteristics. The corresponding 90% CL upper limit on the $e^+e^-\gamma$ background in the data sample is 4.6 events (2 events with $M_{p\bar{p}} < 4.5$ GeV/ c^2).

To compare MC simulation and data for the process $e^+e^- \rightarrow \mu^+\mu^-\gamma$, we use a subsample of events selected with the requirement that both charged particles be identified as muons. Muon identification is based on IFR information, and does not use DIRC or dE/dx information, which are necessary for proton identification. In the data samples with one or two identified protons obtained with the standard χ^2 selection, we select 86 and 2 muon-identified events, respectively. These numbers can be compared with 60 ± 16 and zero events expected from the $e^+e^- \rightarrow \mu^+\mu^-\gamma$ simulation. Taking into account that the ratio of the total number of $\mu^+\mu^-\gamma$ events to those with two identified muons is about two-to-one, we estimate the $\mu^+\mu^-\gamma$ background for the standard selection criteria to be 4.0 ± 2.8 events.

The combined background from the processes $e^+e^- \rightarrow C^+C^-\gamma$, $C = \pi, K, e, \mu$ is less than 0.2% of the number of selected $p\bar{p}\gamma$ candidates, and so can be neglected.

B. Background from $e^+e^- \rightarrow p\bar{p}\pi^0$

The dominant source of background to the $e^+e^- \rightarrow p\bar{p}\gamma$ process arises from $e^+e^- \rightarrow p\bar{p}\pi^0$. A significant frac-

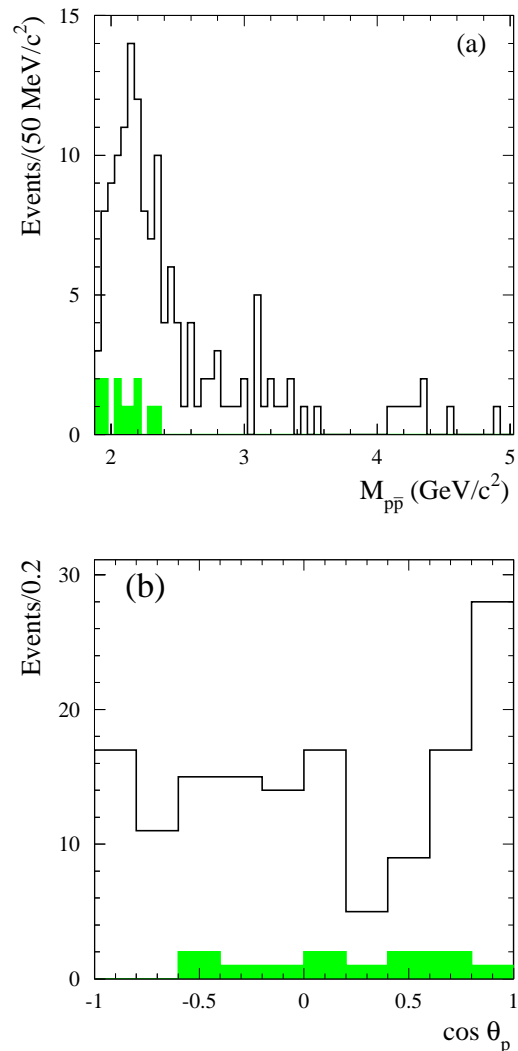


FIG. 5: (a) The $M_{p\bar{p}}$ spectrum and (b) the $\cos\theta_p$ distribution for selected $e^+e^- \rightarrow p\bar{p}\pi^0$ candidates in data. In each figure, the shaded histogram shows the background contribution estimated from the $M_{\gamma\gamma}$ sidebands.

tion of $p\bar{p}\pi^0$ events with an undetected low-energy photon, or with merged photons from the π^0 decay, is reconstructed under the $p\bar{p}\gamma$ hypothesis with a low value of χ^2 , and so cannot be separated from the process under study. This background is studied by selecting a special subsample of events containing two charged particles identified as protons and at least two photons with energy greater than 0.1 GeV, one of which must have c.m. energy above 3 GeV. The two-photon invariant mass is required to be in the range 0.07–0.20 GeV/ c^2 , which is centered on the nominal π^0 mass. A kinematic fit to the $e^+e^- \rightarrow p\bar{p}\gamma\gamma$ hypothesis is then performed. Requirements on the χ^2 of the kinematic fit ($\chi^2 < 25$) and the two-photon invariant mass ($0.1025 < M_{\gamma\gamma} < 0.1675$ GeV/ c^2) are imposed in order to select $e^+e^- \rightarrow p\bar{p}\pi^0$ candidates. The $M_{\gamma\gamma}$ sidebands $0.0700 < M_{\gamma\gamma} < 0.1025$ GeV/ c^2 and

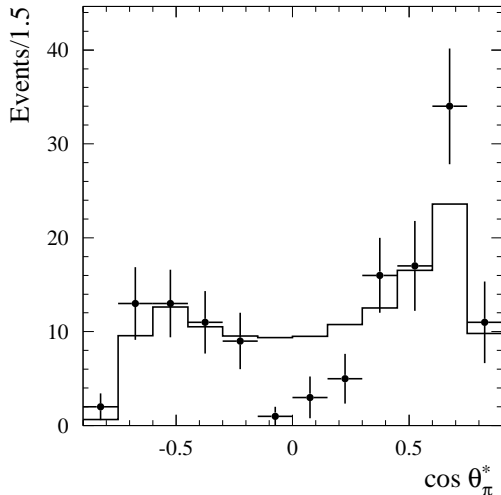


FIG. 6: The $\cos\theta_\pi^*$ distribution for $e^+e^- \rightarrow p\bar{p}\pi^0$ event candidates for data (points with error bars) and simulation (histogram).

$0.1675 < M_{\gamma\gamma} < 0.2000$ GeV/c^2 are used to estimate background. The $M_{p\bar{p}}$ spectra and $\cos\theta_p$ distributions for data events from the signal and sideband $M_{\gamma\gamma}$ regions are shown in Fig. 5. The total number of selected events is 148 in the signal region and 12 in the sidebands. The number of $e^+e^- \rightarrow p\bar{p}\pi^0$ events in the $M_{\gamma\gamma}$ sidebands expected from MC simulation is 5.4.

The $p\bar{p}\pi^0$ selection criteria described above are applied to simulated $e^+e^- \rightarrow q\bar{q}$ events generated with the JETSET program. In the mass region $M_{p\bar{p}} < 5$ GeV/c^2 , the predicted number of $e^+e^- \rightarrow p\bar{p}\pi^0$ events is 120 ± 9 . These events exhibit an enhancement in the $M_{p\bar{p}}$ distribution near the $p\bar{p}$ threshold, similar to that in data. However, the $\cos\theta_p$ distribution of MC events is peaked near $\cos\theta_p = \pm 1$, whereas for the data the distribution is flat. To study the $e^+e^- \rightarrow p\bar{p}\pi^0$ background, the sample of simulated $e^+e^- \rightarrow p\bar{p}\pi^0$ events is generated according to three-body phase space, but with an additional weight proportional to $(M_{p\bar{p}} - 2m_p)^{3/2}$ to imitate the $M_{p\bar{p}}$ distribution observed in data. The resulting generated $\cos\theta_p$ distribution is flat.

In Fig. 6 the $\cos\theta_\pi^*$ distribution for selected data and simulated $e^+e^- \rightarrow p\bar{p}\pi^0$ events is shown, where θ_π^* is the π^0 polar angle in the e^+e^- c.m. frame. It is seen that the data and simulated distributions differ slightly. Since we do not observe a significant variation of the $\cos\theta_\pi^*$ distribution with $M_{p\bar{p}}$ in data, we use the data distribution averaged over $M_{p\bar{p}}$ (Fig. 6) to reweight the $e^+e^- \rightarrow p\bar{p}\pi^0$ simulation.

From the reweighted simulation, we calculate the ratio (K_{MC}) of the $M_{p\bar{p}}$ distribution for events selected with the standard $p\bar{p}\gamma$ criteria to that selected with the $p\bar{p}\pi^0$ criteria. The value of the ratio $K_{\text{MC}}(M_{p\bar{p}})$ varies from 3.4 near the $M_{p\bar{p}}$ threshold to 2.0 at 5 GeV/c^2 . The expected $M_{p\bar{p}}$ spectrum for the $e^+e^- \rightarrow p\bar{p}\pi^0$ background

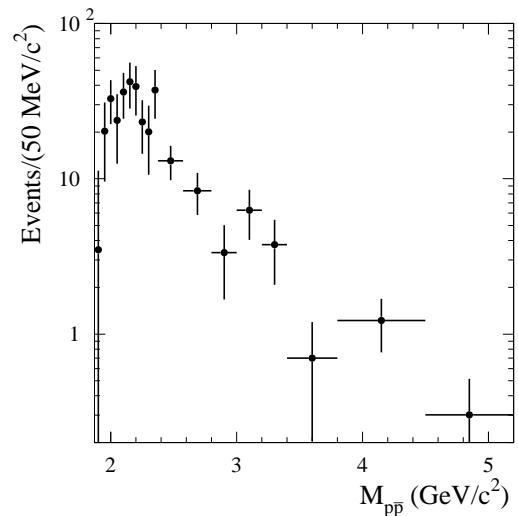


FIG. 7: The expected $M_{p\bar{p}}$ spectrum for $e^+e^- \rightarrow p\bar{p}\pi^0$ events selected with the standard $p\bar{p}\gamma$ criteria. The spectrum is obtained by scaling the data distribution shown in Fig. 5(a) by the factor $K_{\text{MC}}(M_{p\bar{p}})$ described in the text.

satisfying the $p\bar{p}\gamma$ selection criteria is shown in Fig. 7, and is evaluated as $K_{\text{MC}}(M_{p\bar{p}}) \times (dN/dM_{p\bar{p}})_{\text{data}}$, where $(dN/dM_{p\bar{p}})_{\text{data}}$ is the mass distribution for $e^+e^- \rightarrow p\bar{p}\pi^0$ events obtained above (Fig. 5(a)). The number of selected $e^+e^- \rightarrow p\bar{p}\gamma$ candidates and the expected number of $e^+e^- \rightarrow p\bar{p}\pi^0$ background events are given for different $p\bar{p}$ mass ranges in Table II. The background contribution grows from 5% near $p\bar{p}$ threshold to 50% at $M_{p\bar{p}} \approx 4$ GeV/c^2 . All observed $p\bar{p}\gamma$ candidates with $M_{p\bar{p}} > 4.5$ GeV/c^2 are consistent with $p\bar{p}\pi^0$ background.

C. Other sources of background

Other possible background sources are ISR processes with higher final-state multiplicity ($e^+e^- \rightarrow p\bar{p}\pi^0\gamma$, $p\bar{p}2\pi^0\gamma$, ...), and direct e^+e^- annihilation processes other than $e^+e^- \rightarrow p\bar{p}\pi^0$ ($e^+e^- \rightarrow p\bar{p}\eta$, $e^+e^- \rightarrow p\bar{p}2\pi^0$, and so on). All of these processes are simulated by JETSET. The simulation leads to the prediction that the ISR background is 55 ± 6 events, and that the direct annihilation background is 40 ± 5 events. The total predicted background from these two sources is about 1.2% of the number of selected $p\bar{p}\gamma$ candidates. We do not perform a detailed study of these background processes. Their contribution is estimated from data by using the χ^2 sideband region, as described below in Sec. IV D.

D. Background subtraction

Table III summarizes the expected number of background events estimated in the previous sections. The “other ISR” and “ e^+e^- ” columns show the background

TABLE II: The number of selected $p\bar{p}\gamma$ candidates, $N_{p\bar{p}\gamma}$, and the number of background events from the $e^+e^- \rightarrow p\bar{p}\pi^0$ process, $N_{p\bar{p}\pi^0}$, for different ranges of $M_{p\bar{p}}$. The $p\bar{p}$ mass ranges near the J/ψ and $\psi(2S)$ resonances are excluded.

$M_{p\bar{p}}$ (GeV/ c^2)	< 2.50	2.50–3.05	3.15–3.60	3.75–4.50	> 4.5
$N_{p\bar{p}\gamma}$	6695	592	76	29	9
$N_{p\bar{p}\pi^0}$	321 ± 37	66 ± 15	26 ± 9	17 ± 6	6 ± 3

TABLE III: The number of selected $p\bar{p}\gamma$ candidates from the mass region $M_{p\bar{p}} < 4.5$ GeV/ c^2 with $\chi_p^2 < 30$ (N_1) and $30 < \chi_p^2 < 60$ (N_2) for signal and for different background processes; β_i is the ratio N_2/N_1 obtained from simulation. The first column shows the numbers of $p\bar{p}\gamma$ candidates selected in data. The numbers for $e^+e^- \rightarrow p\bar{p}\gamma$ are obtained from data using the background subtraction procedure described in the text.

	data	$p\bar{p}\pi^0$	e^+e^-	Other ISR	$p\bar{p}\gamma$
N_1	8298	448 ± 42	40 ± 5	55 ± 6	7741 ± 113
N_2	560	79 ± 7	76 ± 7	74 ± 7	337 ± 16
β_i		0.175 ± 0.04	1.88 ± 0.29	1.34 ± 0.18	0.0435 ± 0.0020

contributions estimated with JETSET that result from ISR processes, and from e^+e^- annihilation processes other than $e^+e^- \rightarrow p\bar{p}\pi^0$. Because JETSET has not been verified precisely for the rare processes contributing to the $p\bar{p}\gamma$ candidate sample, we use a method of background estimation that is based on the difference in χ^2 distributions for signal and background events. The first and second rows in Table III show the expected numbers of signal and background events with $\chi_p^2 < 30$ (N_1) and $30 < \chi_p^2 < 60$ (N_2). The last row lists β_i , the ratio of N_2 to N_1 . From Table III, it is evident that the coefficient β_i for signal events, and for background events from the processes with higher hadron multiplicity (“ e^+e^- ” and “Other ISR” columns), are very different. This difference can be used to estimate the background from these two sources, as follows. First, the $p\bar{p}\pi^0$ background determined as described in Sec. IV B is subtracted from data. Then, from the corrected numbers of events in the signal and sideband χ^2 regions, N'_1 and N'_2 , the numbers of signal and background (from “ e^+e^- ” and “ISR” sources) events with $\chi_p^2 < 30$ can be calculated:

$$N_{sig} = \frac{N'_1 - N'_2/\beta_{bkg}}{1 - \beta_{p\bar{p}\gamma}/\beta_{bkg}}, \quad (5)$$

$$N_{bkg} = N'_1 - N_{sig},$$

where β_{bkg} is the ratio of the fractions of events in the sideband and signal χ^2 regions averaged over all background processes of the “ e^+e^- ” and “ISR” types. For this coefficient, $\beta_{bkg} = 1.6 \pm 0.3$ is used; it is the average of $\beta_{e^+e^-}$ and β_{ISR} with the uncertainty $(\beta_{e^+e^-} - \beta_{ISR})/2$.

In Table III, it is also evident that $p\bar{p}\gamma$ events dominate the χ^2 sideband region. Therefore, the background is very sensitive to the accuracy of the $\beta_{p\bar{p}\gamma}$ coefficient. In particular, the data-Monte Carlo difference in the χ^2 distribution can lead to a systematic shift of the result. The simulation of the χ^2 distribution for $p\bar{p}\gamma$ events is validated using data and simulated $e^+e^- \rightarrow \mu^+\mu^-\gamma$ events. These are very similar kinematically to the process under

study, and can be selected with negligible background. The ratio of the β coefficients for $e^+e^- \rightarrow \mu^+\mu^-\gamma$ data and simulation is independent of the $\mu^+\mu^-$ mass and is equal to 1.008 ± 0.008 . This ratio is used to correct the $\beta_{p\bar{p}\gamma}$ value obtained from simulation, which varies from 0.043 at $p\bar{p}$ threshold to 0.048 at 4.5 GeV/ c^2 .

With the method described above, the total numbers of $e^+e^- \rightarrow p\bar{p}\gamma$ events (N_{sig}) and background events from “ e^+e^- ” and “ISR” sources (N_{bkg}) in the signal region are found to be $7741 \pm 95 \pm 62$ and $109 \pm 16 \pm 25$, respectively. The main source of the systematic uncertainty on N_{sig} is the uncertainty in the $p\bar{p}\pi^0$ background. The number of background events is in good agreement with the estimate from simulation, $(40 \pm 5) + (55 \pm 6) = 95 \pm 8$. The total background in the $\chi_p^2 < 30$ region is 531 ± 51 events, which is about 7% of the number of signal events.

The background subtraction procedure is performed in each $p\bar{p}$ mass interval. The number of selected events for each interval after background subtraction and unfolding event migration between intervals (see Sec. VII) is listed in Table VI. The events from J/ψ and $\psi(2S)$ decays are subtracted from the contents of the corresponding intervals (see Sec. VIII).

V. ANGULAR DISTRIBUTIONS

The modulus of the ratio of the electric and magnetic form factors can be extracted from an analysis of the distribution of θ_p , the angle between the proton momentum in the $p\bar{p}$ rest frame and the momentum of the $p\bar{p}$ system in the e^+e^- c.m. frame. This distribution is given by

$$\frac{dN}{d \cos \theta_p} = A \left(H_M(\cos \theta_p, M_{p\bar{p}}) + \left| \frac{G_E}{G_M} \right|^2 H_E(\cos \theta_p, M_{p\bar{p}}) \right). \quad (6)$$

TABLE IV: The number of selected $p\bar{p}\gamma$ candidates (N) and the number of background events (N_{bkg}) for each $p\bar{p}$ mass interval; $|G_E/G_M|$ is the fitted ratio of form factors.

$M_{p\bar{p}}, \text{GeV}/c^2$	N	N_{bkg}	$ G_E/G_M $
1.877–1.950	1162	19 ± 10	$1.36^{+0.15+0.05}_{-0.14-0.04}$
1.950–2.025	1290	53 ± 16	$1.48^{+0.16+0.06}_{-0.14-0.05}$
2.025–2.100	1328	63 ± 14	$1.39^{+0.15+0.07}_{-0.14-0.07}$
2.100–2.200	1444	118 ± 28	$1.26^{+0.14+0.10}_{-0.13-0.09}$
2.200–2.400	1160	126 ± 26	$1.04^{+0.16+0.10}_{-0.16-0.10}$
2.400–3.000	879	122 ± 22	$1.04^{+0.24+0.15}_{-0.25-0.15}$

The functions $H_M(\cos\theta_p, M_{p\bar{p}})$ and $H_E(\cos\theta_p, M_{p\bar{p}})$ do not have an analytic form, and so are determined using MC simulation. To do this, two samples of $e^+e^- \rightarrow p\bar{p}\gamma$ events are generated, one with $G_E = 0$ and the other with $G_M = 0$. The functions obtained are close to the $1 + \cos^2\theta_p$ and $\sin^2\theta_p$ functions describing angular distributions for the magnetic and electric form factors in the case of $e^+e^- \rightarrow p\bar{p}$.

The observed angular distributions are fit in six ranges of $p\bar{p}$ invariant mass from threshold to $3 \text{ GeV}/c^2$. The fit intervals, the corresponding numbers of selected events, and the estimated numbers of background events are listed in Table IV. For each $p\bar{p}$ mass interval and each angular interval the background is subtracted using the procedure described in Section IV D. The angular distributions obtained are shown in Fig. 8. The distributions are fit to Eq. (6) with two free parameters: A (the overall normalization) and $|G_E/G_M|$. The functions H_M and H_E are replaced by the histograms obtained from MC simulation with the $p\bar{p}\gamma$ selection criteria applied. To account for differences between the $p\bar{p}$ mass distributions of $p\bar{p}\gamma$ events in data and MC simulation, the histograms H_M and H_E are recalculated using weighted events. The weights are obtained from the ratio of the $p\bar{p}$ mass distributions in data and simulation. In principle, the weights for H_M and H_E differ due to the different mass dependences of G_M and G_E . A first approximation uses $G_M = G_E$. The fitted values of $|G_E/G_M|$ are then used in the next approximation to recalculate H_M and H_E . The second iteration leads to a small change (less than 2%) in the fitted values, and the procedure converges after a third iteration.

The simulated angular distributions are corrected to account for the differences between data and simulation in particle identification, tracking, and photon efficiency. These corrections are discussed in detail in the next section. The angular dependence of the detection efficiency calculated with MC simulation before and after the corrections is shown in Fig. 9. The deviations from uniform efficiency, which do not exceed 10%, arise from the momentum dependence of proton/antiproton particle identification efficiency.

The fits of the histograms to the angular distributions

are shown in Fig. 8; the values of $|G_E/G_M|$ obtained are listed in Table IV and shown in Fig. 10. The curve in Fig. 10 [$1 + ax/(1 + bx^3)$, where $x = M_{p\bar{p}} - 2m_p \text{ GeV}/c^2$] is used in the iteration procedure to calculate the weight. The quoted errors on $|G_E/G_M|$ are statistical and systematic, respectively. The dominant contribution to the systematic error is due to the uncertainty in the $p\bar{p}\pi^0$ background.

The only previous measurement of the $|G_E/G_M|$ ratio was performed in the PS170 experiment [11]. The ratio was measured at five points between $1.92 \text{ GeV}/c^2$ and $2.04 \text{ GeV}/c^2$ with an accuracy of 30–40% (see Fig. 10). For all points it was found to be consistent with unity. The average of the PS170 measurements evaluated under the assumption that the errors are purely statistical is 0.90 ± 0.14 . The *BABAR* results are significantly larger for $M_{p\bar{p}} < 2.1 \text{ GeV}/c^2$, and extend the measurements up to $3 \text{ GeV}/c^2$.

In addition, we search for an asymmetry in the proton angular distribution. The lowest-order one-photon mechanism for proton-antiproton production predicts a symmetric angular distribution. An asymmetry arises from higher-order contributions, in particular, from two-photon exchange. Two-photon exchange is discussed (see, for example, Ref. [23]) as a possible source of the difference observed in ep scattering between the G_E/G_M measurements obtained with two different experimental techniques, namely the Rosenbluth method [24], which uses the analysis of angular distributions, and the polarization method [25–27], which is based on the measurement of the ratio of the transverse and longitudinal polarization of the recoil proton.

A search for an asymmetry using previous *BABAR* $e^+e^- \rightarrow p\bar{p}\gamma$ data [14] is described in Ref. [28]. No asymmetry was observed within the statistical error of 2%. It should be noted that the authors of Ref. [28] did not take into account the angular asymmetry of the detection efficiency, which is seen in Fig. 9 and in a similar plot in Ref. [14]. To measure the asymmetry we use the data with $p\bar{p}$ mass less than $3 \text{ GeV}/c^2$. The $\cos\theta_p$ distribution is fitted as described above, and the result is shown in Fig. 11. Since the MC simulation uses a model with one-photon exchange, the asymmetry in the fitted histogram is due to asymmetry in the detection efficiency. To remove detector effects we take the ratio of the data distribution to the fitted simulated distribution. This ratio is shown in Fig. 12. A fit of a linear function to the data yields a slope parameter value $-0.041 \pm 0.026 \pm 0.005$. The systematic error on the slope is estimated conservatively as the maximum slope given by an efficiency correction. The correction for the data-MC simulation difference in antiproton nuclear interactions (see Sec. VI) is found to yield the largest angular variation.

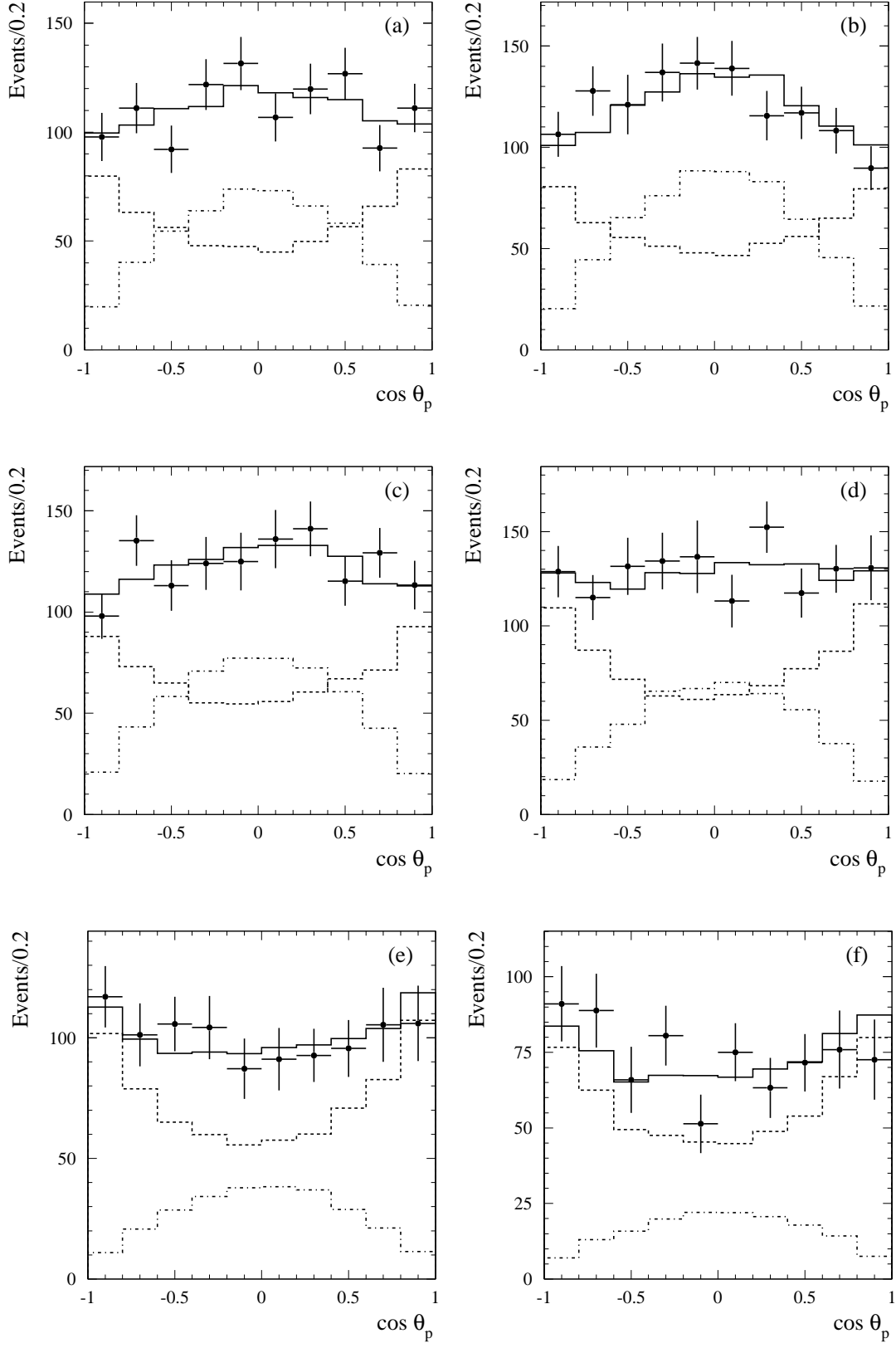


FIG. 8: The $\cos \theta_p$ distributions for different $p\bar{p}$ mass regions: (a) 1.877–1.950 GeV/c^2 , (b) 1.950–2.025 GeV/c^2 , (c) 2.025–2.100 GeV/c^2 , (d) 2.100–2.200 GeV/c^2 , (e) 2.200–2.400 GeV/c^2 , (f) 2.400–3.000 GeV/c^2 . The points with error bars show the data distributions after background subtraction. The histograms result from the fits: the dashed histograms correspond to the magnetic form factor contributions and the dot-dashed histograms to the electric form factor contributions.

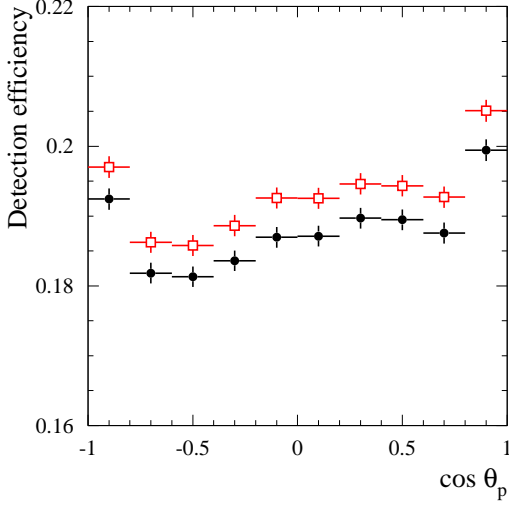


FIG. 9: The angular dependence of the detection efficiency for simulated events with $M_{p\bar{p}} < 2.5 \text{ GeV}/c^2$ before (open squares) and after (filled circles) correction for data-simulation differences in detector response.

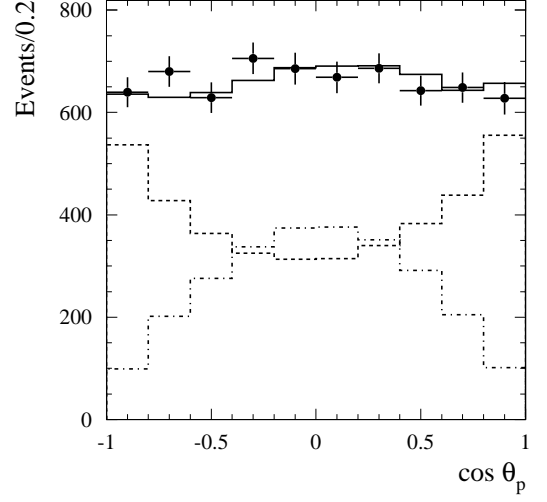


FIG. 11: The $\cos \theta_p$ distribution for the mass region from threshold to $3 \text{ GeV}/c^2$. The points with error bars show the data distribution after background subtraction; the solid histogram is the fit result. The dashed and dot-dashed histograms show the contributions of the terms corresponding to the magnetic and electric form factors, respectively.

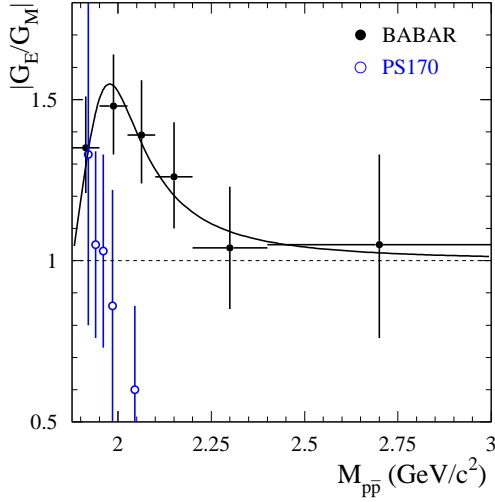


FIG. 10: The measured $|G_E/G_M|$ mass dependence. Filled circles depict *BABAR* data. Open circles show PS170 data [11]. The curve is the the result of the fit described in the text.

We then calculate the integral asymmetry

$$\begin{aligned} A_{\cos \theta_p} &= \frac{\sigma(\cos \theta_p > 0) - \sigma(\cos \theta_p < 0)}{\sigma(\cos \theta_p > 0) + \sigma(\cos \theta_p < 0)} \\ &= -0.025 \pm 0.014 \pm 0.003, \end{aligned} \quad (7)$$

where $\sigma(\cos \theta_p > 0)$ and $\sigma(\cos \theta_p < 0)$ are the cross sections for $e^+e^- \rightarrow p\bar{p}\gamma$ events with $M_{p\bar{p}} < 3 \text{ GeV}/c^2$ integrated over the angular regions with $\cos \theta_p > 0$ and $\cos \theta_p < 0$, respectively. The fitted slope value and the integral asymmetry are consistent with zero. The value of the asymmetry extracted from experiment depends on

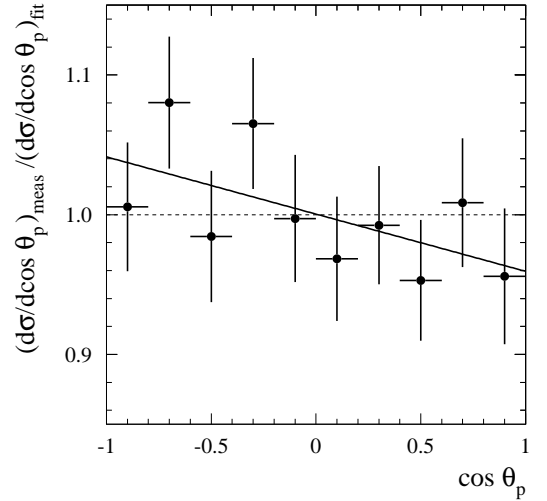


FIG. 12: The ratio of the data distribution from Fig. 11 to the fitted simulated distribution. The line shows the result of the fit of a linear function to the data points.

the selection criteria used, in particular, on the effective energy limit for an extra photon emitted from the initial or final state. In our analysis, this limit is determined by the condition $\chi_p^2 < 30$, and is about 100 MeV .

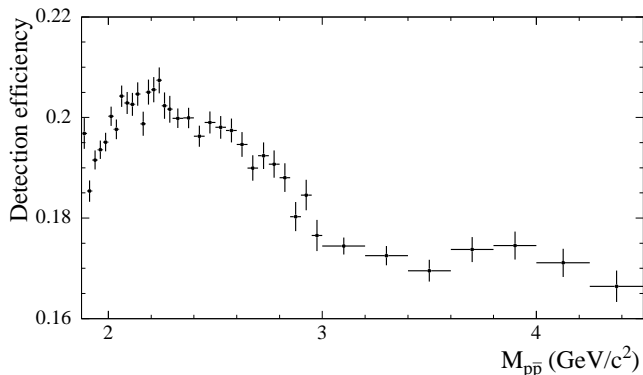


FIG. 13: The $p\bar{p}$ mass dependence of the detection efficiency obtained from MC simulation.

VI. DETECTION EFFICIENCY

The detection efficiency, which is determined using Monte Carlo simulation, is the ratio of true $p\bar{p}$ mass distributions computed after and before applying the selection criteria. Since the $e^+e^- \rightarrow p\bar{p}\gamma$ differential cross section depends on two form factors, the detection efficiency cannot be determined in a model-independent way. We use a model with the $|G_E/G_M|$ ratio obtained from the fits to the experimental angular distributions (curve in Fig. 10) for $M_{p\bar{p}} < 3 \text{ GeV}/c^2$, and with $|G_E/G_M| = 1$ for higher masses. The detection efficiency obtained by using this model is shown in Fig. 13. The error in the detection efficiency due to the model is determined from the uncertainty in the $|G_E/G_M|$ ratio: for $M_{p\bar{p}} < 3 \text{ GeV}/c^2$ the variation of the ratio within its experimental uncertainties leads to a 1% change in the detection efficiency. This is taken as the model-related uncertainty. For the mass region above $3 \text{ GeV}/c^2$, where the $|G_E/G_M|$ ratio is not measured, the model uncertainty is taken as the maximum difference between the detection efficiencies corresponding to setting $G_E = 0$ or setting $G_M = 0$, and the efficiency calculated with the model described above. This yields a 4% uncertainty estimate.

The efficiency determined from MC simulation (ε_{MC}) must be corrected to account for data-MC simulation differences in detector response:

$$\varepsilon = \varepsilon_{\text{MC}} \prod (1 + \delta_i), \quad (8)$$

where the δ_i are efficiency corrections for each of several effects. These corrections are discussed in detail below and summarized in Table V.

Inaccuracies in the simulation of angular and momentum resolution and radiative corrections may account for data-MC differences in the fraction of events rejected by the requirement $\chi_p^2 < 30$. The efficiency correction for this effect is estimated by comparing data and simulated χ^2 distributions for the $e^+e^- \rightarrow \mu^+\mu^-\gamma$ process, which has kinematics similar to the process under study. An exclusive $e^+e^- \rightarrow \mu^+\mu^-\gamma$ sample is selected by re-

quiring that both charged tracks be identified as muons. The ratio of the number of selected muon events with $\chi_\mu^2 > 30$ and $\chi_\mu^2 < 30$ varies from 0.30 to 0.37 in the $M_{p\bar{p}}$ range from threshold to $4.5 \text{ GeV}/c^2$. To characterize data-MC simulation differences in the χ^2 distribution, a double ratio (κ) is calculated as the ratio of $N(\chi_\mu^2 > 30)/N(\chi_\mu^2 < 30)$ obtained from data to the same quantity obtained from MC simulation. The value of the double ratio varies from 1.02 to 1.06 in the $M_{p\bar{p}}$ range from threshold to $4.5 \text{ GeV}/c^2$. The efficiency correction δ_i (with $i = 1$) for the χ_p^2 cut is calculated as

$$\delta_1 = \frac{N(\chi_p^2 < 30) + N(\chi_p^2 > 30)}{N(\chi_p^2 < 30) + \kappa N(\chi_p^2 > 30)} - 1, \quad (9)$$

where $N(\chi_p^2 < 30)$ and $N(\chi_p^2 > 30)$ are the numbers of simulated $p\bar{p}\gamma$ events with $\chi_p^2 < 30$ and $\chi_p^2 > 30$, respectively. The values of the efficiency correction δ_1 for different $p\bar{p}$ invariant-mass values are listed in Table V.

The effect of the $\chi_K^2 > 30$ requirement is studied using $e^+e^- \rightarrow J/\psi\gamma \rightarrow p\bar{p}\gamma$ events. The J/ψ yield is determined using the sideband subtraction method. The event losses are found to be $(1.5 \pm 0.4)\%$ in data and $(1.2 \pm 0.1)\%$ in MC simulation. As the data and simulated values are in good agreement, there is no need to introduce any efficiency correction for the $\chi_K^2 > 30$ requirement. The systematic uncertainty associated with this criterion is 0.4%.

Another possible source of data-MC simulation differences is due to unreconstructed tracks. Two dominant effects leading to track loss in $p\bar{p}\gamma$ events are track overlap in the DCH and nuclear interaction of protons and antiprotons in the material before the SVT and DCH.

The effect of track overlap can be observed in the distribution of the parameter $\Delta\varphi_\pm = \varphi_+ - \varphi_-$, where φ_+ and φ_- are the azimuthal angles at the production vertex of positive and negative tracks, respectively. The detection efficiency for simulated $e^+e^- \rightarrow p\bar{p}\gamma$ events as a function of $\Delta\varphi_\pm$ is shown in Fig. 14.

The z -component of the *BABAR* magnetic field is in the direction of the positive z -axis, so that in the $x - y$ plane viewed from positive z positively charged tracks experience clockwise bending, while negatively charged tracks are bent counter-clockwise. As a result, events with $\Delta\varphi_\pm > 0$ have a “fishtail” two-track configuration in which the tracks tend to overlap initially. This results in the dip in efficiency which is clearly seen at $\Delta\varphi_\pm \sim 0.1$ rad. The ratio of the number of events with $\Delta\varphi_\pm > 0$ to that with $\Delta\varphi_\pm < 0$ can be used to estimate the efficiency loss due to track overlap. This efficiency loss reaches about 10% near $p\bar{p}$ threshold and decreases to a negligible level for $M_{p\bar{p}}$ above $2.4 \text{ GeV}/c^2$. The effect is reproduced reasonably well by the MC simulation; data-MC simulation differences in the efficiency loss averaged over the mass region of maximum inefficiency, $M_{p\bar{p}} < 2.3 \text{ GeV}/c^2$, is about $(1.2 \pm 1.3)\%$. We introduce no correction for this difference. For the mass region $M_{p\bar{p}} < 2.3 \text{ GeV}/c^2$, where the effect is large, a systematic uncer-

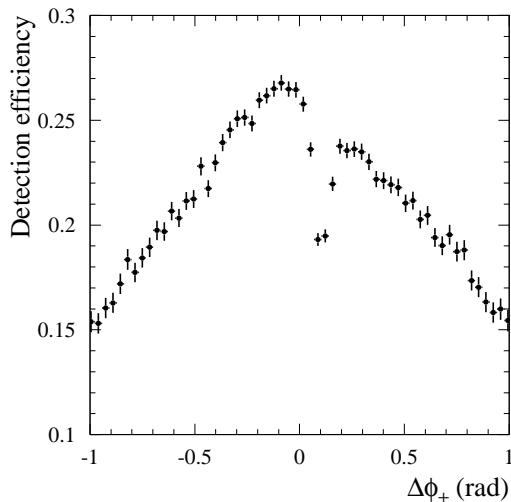


FIG. 14: The detection efficiency for $e^+e^- \rightarrow p\bar{p}\gamma$ events as a function of $\Delta\phi_{\pm}$ obtained from MC simulation.

tainty of 1.5% is assigned to the measured cross section.

Simulation shows that nuclear interaction leads to the loss of approximately 6% of the $e^+e^- \rightarrow p\bar{p}\gamma$ events. For data-MC simulation comparison, a specially selected event sample with $\Lambda(\bar{\Lambda})$ decaying into $p(\bar{p})\pi$ is used. The Λ candidates are selected by imposing requirements on the $p\pi$ invariant mass and Λ flight distance. The amount of material before the SVT (1.5% of a nuclear interaction length) is comparable to the amount of material between the SVT and the DCH (1.4% of a nuclear interaction length). The probability of track losses between the SVT and the DCH is measured by using the $\Lambda(\bar{\Lambda})$ sample. The data and simulation probabilities are found to be in agreement for protons. A substantial difference is observed for antiprotons, which is consistent with a large (a factor of 2.6 ± 1.0) overestimation of the antiproton annihilation cross section in simulation. This difference in the antiproton annihilation cross section in data and simulation leads to a correction of about $(1.0 \pm 0.4)\%$ to the detection efficiency for $p\bar{p}\gamma$ events.

We also incorporate a systematic uncertainty due to data-MC simulation differences in track reconstruction, which is estimated to be 0.24% per track.

The data-MC simulation difference in particle identification is studied using events with a $J/\psi \rightarrow p\bar{p}$ decay. Due to the narrow J/ψ width and hence low background, the number of $J/\psi \rightarrow p\bar{p}$ decays may be determined using selections with either one or two identified protons. The background from non- J/ψ events is subtracted using sidebands. The p/\bar{p} identification probabilities are determined as functions of the p/\bar{p} momenta by calculating the ratio of the number of events with both the proton and the antiproton identified to the number of events with only one identified proton or antiproton. The ratio of data-MC identification probabilities is used to reweight selected simulated events and calculate efficiency correc-

tions. The correction is about $-(1.9 \pm 2.0)\%$ and is practically independent of $p\bar{p}$ mass. The error in the correction is determined from the statistical uncertainty on the number of selected J/ψ events.

An additional correction must be applied to the photon detection efficiency. There are two main sources of this correction. The first is due to data-MC simulation differences in the probability of photon conversion in the detector material before the DCH, and the second results from the effect of dead calorimeter channels. A sample of $e^+e^- \rightarrow \mu^+\mu^-\gamma$ events is used to determine the calorimeter photon inefficiency in data. Events with exactly two oppositely charged particle tracks identified as muons are selected, and a one-constraint kinematic fit is performed, in which the recoil mass against the muon pair is constrained to be zero. A tight requirement on the χ^2 of the kinematic fit selects events with only one photon in the final state. The photon direction is determined from the fit, and the detection inefficiency is calculated as the ratio of the number of events not satisfying the $E_{\gamma}^* > 3$ GeV criterion, to the total number of selected $\mu^+\mu^-\gamma$ events. The photon inefficiency obtained is 3.3%, to be compared to the 2% inefficiency from the $e^+e^- \rightarrow \mu^+\mu^-\gamma$ simulation. The data-MC simulation difference in the probability of photon conversion is also studied using $e^+e^- \rightarrow \mu^+\mu^-\gamma$ events. In addition to two identified muons, we require that an event contain a converted-photon candidate, i.e., a pair of oppositely charged tracks with e^+e^- invariant mass close to zero, momentum directed along the expected photon direction, and forming a secondary vertex well-separated from the interaction region. The observed data-MC difference in the probability of photon conversion is $-(0.41 \pm 0.01)\%$. The data-MC differences in the calorimeter inefficiency for photons and the probability of photon conversion are determined as functions of the photon polar angle, and used to reweight the simulated events and calculate efficiency corrections. The total correction due to data-MC simulation differences in the photon detection inefficiency is found to vary from of $-(1.9 \pm 0.1)\%$ near the $p\bar{p}$ threshold to $-(1.7 \pm 0.1)\%$ at 3 GeV/ c^2 and higher masses.

The quality of the simulation of trigger efficiency is also studied. The overlap of the samples of events satisfying different trigger criteria, and the independence of these triggers, are used to measure trigger efficiency. The difference in trigger efficiency between data and MC simulation decreases from $-(0.65 \pm 0.20)\%$ near $p\bar{p}$ threshold to $-(0.13 \pm 0.10)\%$ for $p\bar{p}$ masses above 2.2 GeV/ c^2 . An additional systematic uncertainty of about 0.5% is introduced to take into account the possibly imperfect simulation of inefficiency of the offline filters that provide background suppression before full event reconstruction.

All efficiency corrections are summarized in Table V, and the corrected detection efficiency values are listed in Table VI. The uncertainty in detection efficiency includes simulation statistical error, model uncertainty, and the uncertainty on the efficiency correction.

TABLE V: The values of the different efficiency corrections δ_i for $p\bar{p}$ invariant mass 1.9, 3.0, and 4.5 GeV/c^2 .

effect	$\delta_i(1.9), \%$	$\delta_i(3), \%$	$\delta_i(4.5), \%$
$\chi_p^2 < 30$	-0.5 ± 0.1	-0.9 ± 0.1	-1.5 ± 0.2
$\chi_K^2 > 30$	0.0 ± 0.4	0.0 ± 0.4	0.0 ± 0.4
track overlap	0.0 ± 1.5	–	–
nuclear interaction	0.8 ± 0.4	1.1 ± 0.4	1.0 ± 0.4
track reconstruction	0.0 ± 0.5	0.0 ± 0.5	0.0 ± 0.5
PID	-1.9 ± 2.0	-1.9 ± 2.0	-1.9 ± 2.0
photon inefficiency	-1.9 ± 0.1	-1.7 ± 0.1	-1.7 ± 0.1
trigger and filters	-0.7 ± 0.6	-0.1 ± 0.5	-0.1 ± 0.5
total	-4.2 ± 2.6	-3.5 ± 2.2	-4.2 ± 2.2

VII. THE $e^+e^- \rightarrow p\bar{p}$ CROSS SECTION AND THE PROTON FORM FACTOR

The cross section for $e^+e^- \rightarrow p\bar{p}$ is calculated from the $p\bar{p}$ mass spectrum using the expression

$$\sigma_{p\bar{p}}(M_{p\bar{p}}) = \frac{(dN/dM_{p\bar{p}})_{corr}}{\varepsilon R dL/dM_{p\bar{p}}}, \quad (10)$$

where $(dN/dM_{p\bar{p}})_{corr}$ is the mass spectrum corrected for resolution effects, $dL/dM_{p\bar{p}}$ is the ISR differential luminosity, $\varepsilon(M_{p\bar{p}})$ is the detection efficiency as a function of mass, and R is a radiative correction factor accounting for the Born mass spectrum distortion due to emission of extra photons by the initial electron and positron. The ISR luminosity is calculated using the total integrated luminosity L and the integral over $\cos\theta_\gamma^*$ of the probability density function for ISR photon emission (Eq. (2)):

$$\frac{dL}{dM_{p\bar{p}}} = \frac{\alpha}{\pi x} \left((2 - 2x + x^2) \log \frac{1+B}{1-B} - x^2 C \right) \frac{2M_{p\bar{p}}}{s} L. \quad (11)$$

Here $B = \cos\theta_0^*$, and θ_0^* determines the range of polar angles for the ISR photon in the e^+e^- c.m. frame: $\theta_0^* < \theta_\gamma^* < 180^\circ - \theta_0^*$. In our case $\theta_0^* = 20^\circ$, since we determine detector efficiency using simulation with $20^\circ < \theta_\gamma^* < 160^\circ$. The values of ISR luminosity integrated over the $M_{p\bar{p}}$ intervals are listed in Table VI.

The radiative correction factor R is determined from MC simulation at the generator level, with no detector simulation. The $p\bar{p}$ mass spectrum is generated using only the pure Born amplitude for the process $e^+e^- \rightarrow p\bar{p}\gamma$, and then using a model with higher-order radiative corrections included by means of the structure function method [18]. The radiative correction factor, evaluated as the ratio of the second spectrum to the first, varies from 1.001 at $p\bar{p}$ threshold to 1.02 at $M_{p\bar{p}} = 4.5 \text{ GeV}/c^2$.

The value of R depends on the requirement on the invariant mass of the $p\bar{p}\gamma$ system. The value of R obtained in our case corresponds to the requirement $M_{p\bar{p}\gamma} > 8 \text{ GeV}/c^2$ imposed in the simulation. The theoretical uncertainty on the radiative correction calculation by the structure function method does not exceed 1% [18]. The

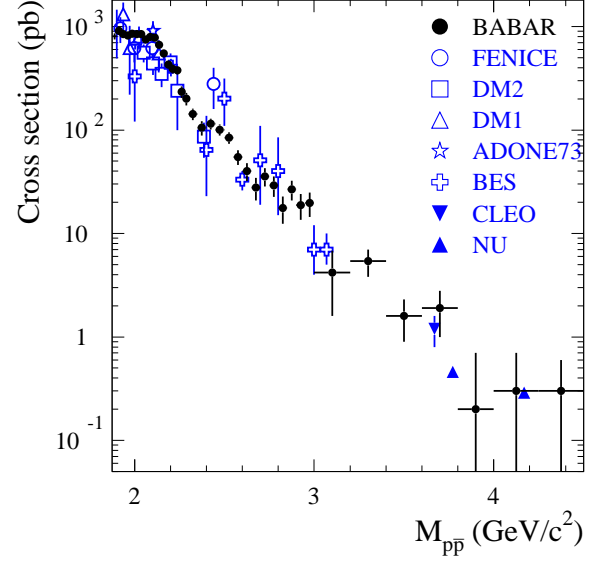


FIG. 15: The $e^+e^- \rightarrow p\bar{p}$ cross section measured in this analysis and in other e^+e^- experiments: FENICE[6], DM2[5], DM1[4], ADONE73[7], BES[8], CLEO[9], NU[10]. The contributions of $J/\psi \rightarrow p\bar{p}$ and $\psi(2S) \rightarrow p\bar{p}$ decays to the BABAR measurement have been subtracted.

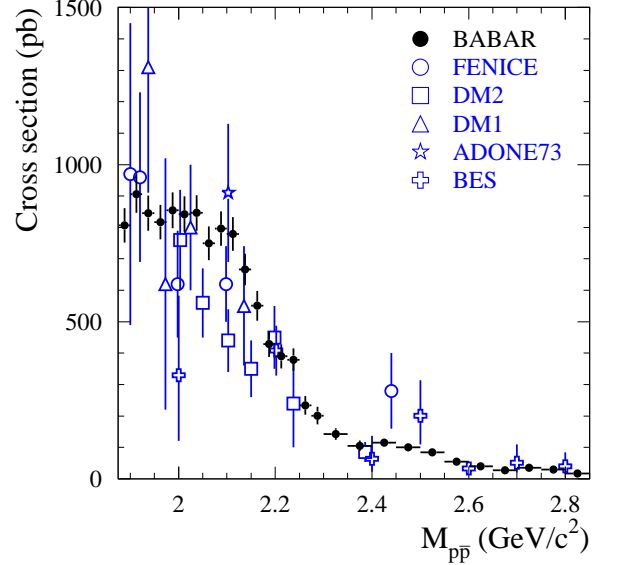


FIG. 16: The $e^+e^- \rightarrow p\bar{p}$ cross section near threshold measured in this analysis and in other e^+e^- experiments: FENICE[6], DM2[5], DM1[4], ADONE73[7], BES[8].

calculated radiative correction factor does not take into account vacuum polarization; the contribution of the latter is included in the measured cross section.

The resolution-corrected mass spectrum is obtained by unfolding the mass resolution from the measured mass spectrum. Using MC simulation, a migration matrix,

TABLE VI: The $p\bar{p}$ invariant-mass interval ($M_{p\bar{p}}$), number of selected events (N) after background subtraction and mass migration, detection efficiency (ε), ISR luminosity (L), measured cross section ($\sigma_{p\bar{p}}$), and $|F_p|$, the effective form factor for $e^+e^- \rightarrow p\bar{p}$. The contributions from $J/\psi \rightarrow p\bar{p}$ and $\psi(2S) \rightarrow p\bar{p}$ decays have been subtracted. The quoted uncertainties on N and σ are statistical and systematic, respectively. For the form factor, the combined uncertainty is listed.

$M_{p\bar{p}}$ (GeV/ c^2)	N	ε	L (pb $^{-1}$)	$\sigma_{p\bar{p}}$ (pb)	$ F_p $
1.877–1.900	351 ± 20 ± 4	0.189 ± 0.006	2.33	806 ± 46 ± 30	0.424 ± 0.014
1.900–1.925	403 ± 22 ± 4	0.178 ± 0.006	2.52	906 ± 50 ± 32	0.355 ± 0.012
1.925–1.950	394 ± 22 ± 5	0.184 ± 0.006	2.56	845 ± 47 ± 31	0.309 ± 0.010
1.950–1.975	390 ± 22 ± 5	0.186 ± 0.006	2.60	817 ± 46 ± 30	0.286 ± 0.010
1.975–2.000	418 ± 24 ± 5	0.187 ± 0.006	2.63	854 ± 48 ± 31	0.281 ± 0.009
2.000–2.025	429 ± 24 ± 5	0.192 ± 0.006	2.67	842 ± 48 ± 30	0.271 ± 0.009
2.025–2.050	433 ± 24 ± 6	0.191 ± 0.006	2.71	846 ± 48 ± 31	0.266 ± 0.009
2.050–2.075	402 ± 24 ± 7	0.197 ± 0.006	2.75	750 ± 45 ± 28	0.247 ± 0.009
2.075–2.100	430 ± 25 ± 6	0.196 ± 0.006	2.79	796 ± 46 ± 29	0.252 ± 0.009
2.100–2.125	426 ± 25 ± 6	0.195 ± 0.006	2.83	779 ± 45 ± 29	0.247 ± 0.008
2.125–2.150	373 ± 24 ± 8	0.197 ± 0.006	2.86	666 ± 43 ± 27	0.227 ± 0.009
2.150–2.175	304 ± 22 ± 8	0.192 ± 0.006	2.90	551 ± 41 ± 24	0.206 ± 0.009
2.175–2.200	247 ± 20 ± 8	0.198 ± 0.006	2.94	429 ± 35 ± 20	0.182 ± 0.009
2.200–2.225	228 ± 20 ± 8	0.198 ± 0.006	2.98	390 ± 33 ± 19	0.173 ± 0.008
2.225–2.250	227 ± 19 ± 6	0.200 ± 0.006	3.02	379 ± 32 ± 16	0.171 ± 0.008
2.250–2.275	139 ± 16 ± 6	0.195 ± 0.006	3.06	234 ± 27 ± 13	0.134 ± 0.009
2.275–2.300	120 ± 15 ± 6	0.195 ± 0.006	3.10	201 ± 25 ± 12	0.125 ± 0.009
2.300–2.350	173 ± 17 ± 13	0.193 ± 0.005	6.32	143 ± 14 ± 12	0.106 ± 0.007
2.350–2.400	130 ± 15 ± 13	0.193 ± 0.005	6.48	105 ± 12 ± 11	0.091 ± 0.007
2.400–2.450	143 ± 15 ± 5	0.190 ± 0.005	6.64	115 ± 12 ± 6	0.096 ± 0.006
2.450–2.500	131 ± 15 ± 5	0.192 ± 0.005	6.80	101 ± 11 ± 5	0.091 ± 0.006
2.500–2.550	111 ± 13 ± 4	0.191 ± 0.005	6.97	84 ± 10 ± 4	0.084 ± 0.005
2.550–2.600	74 ± 11 ± 4	0.191 ± 0.005	7.14	55 ± 8 ± 3	0.069 ± 0.006
2.600–2.650	55 ± 10 ± 3	0.188 ± 0.005	7.31	40 ± 8 ± 3	0.060 ± 0.006
2.650–2.700	38 ± 9 ± 3	0.183 ± 0.005	7.48	28 ± 6 ± 3	0.050 ± 0.006
2.700–2.750	50 ± 9 ± 3	0.186 ± 0.005	7.66	36 ± 7 ± 3	0.058 ± 0.006
2.750–2.800	42 ± 9 ± 3	0.184 ± 0.005	7.84	29 ± 6 ± 3	0.053 ± 0.006
2.800–2.850	25 ± 7 ± 2	0.181 ± 0.005	8.01	18 ± 5 ± 1	0.042 ± 0.006
2.850–2.900	38 ± 8 ± 2	0.174 ± 0.005	8.20	27 ± 6 ± 2	0.052 ± 0.006
2.900–2.950	28 ± 7 ± 2	0.178 ± 0.005	8.38	19 ± 5 ± 2	0.044 ± 0.006
2.950–3.000	29 ± 7 ± 2	0.170 ± 0.005	8.57	20 ± 5 ± 2	0.046 ± 0.006
3.000–3.200	25 ± 12 ± 9	0.168 ± 0.008	36.19	4.2 ± 2.0 ± 1.6	0.022 ± 0.007
3.200–3.400	36 ± 8 ± 7	0.166 ± 0.008	39.40	5.4 ± 1.2 ± 1.1	0.027 ± 0.004
3.400–3.600	11 ± 4 ± 2	0.163 ± 0.008	42.81	1.6 ± 0.6 ± 0.3	0.015 ± 0.003
3.600–3.800	15 ± 6 ± 2	0.167 ± 0.008	46.44	1.9 ± 0.8 ± 0.3	0.018 ± 0.004
3.800–4.000	1 ± 3 ± 2	0.168 ± 0.008	50.33	0.2 ± 0.4 ± 0.2	0.005 ± 0.005
4.000–4.250	4 ± 3 ± 2	0.164 ± 0.008	68.83	0.3 ± 0.3 ± 0.2	0.008 ^{+0.004} _{-0.008}
4.250–4.500	3 ± 4 ± 2	0.160 ± 0.008	76.00	0.3 ± 0.3 ± 0.2	0.008 ^{+0.004} _{-0.008}

A_i , is obtained, which represents the probability that an event with true mass ($M_{p\bar{p}}^{true}$) in mass interval j is reconstructed in interval i :

$$\left(\frac{dN}{dM_{p\bar{p}}}\right)_i^{rec} = \sum_j A_{ij} \left(\frac{dN}{dM_{p\bar{p}}}\right)_j^{true}. \quad (12)$$

The mass resolution changes from 1.5 MeV/ c^2 near threshold to 12 MeV/ c^2 at $M_{p\bar{p}} = 3$ GeV/ c^2 and 22 MeV/ c^2 at 4.5 GeV/ c^2 . Since the chosen mass interval width significantly exceeds the resolution for all $p\bar{p}$ masses, the migration matrix is nearly diagonal, with the values of diagonal elements ~ 0.9 , and next-to-diagonal ~ 0.05 . We unfold the mass spectrum by applying the inverse of the migration matrix to the measured spectrum.

The procedure changes the shape of the mass distribution insignificantly, but increases the uncertainties (by $\approx 20\%$) and their correlations.

After applying the migration matrix, the number of events in each mass interval is listed in Table VI. The quoted errors are statistical and systematic, respectively. The latter is due to the uncertainty in background subtraction. The calculated cross section for $e^+e^- \rightarrow p\bar{p}$ is shown in Fig. 15 and listed in Table VI. For mass intervals 3–3.2 GeV/ c^2 and 3.6–3.8 GeV/ c^2 , the nonresonant cross section is quoted after excluding the J/ψ and $\psi(2S)$ contributions (see Sec. VIII). The errors quoted are statistical and systematic. The systematic uncertainty includes the uncertainty on the number of signal events, detection efficiency, the total integrated luminosity (1%), and the

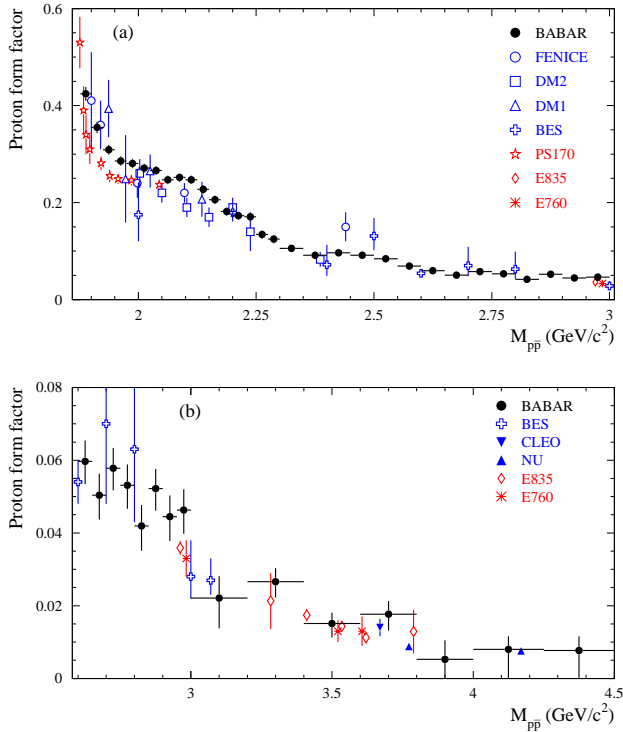


FIG. 17: The proton effective form factor measured in this analysis, in other e^+e^- experiments, and in $p\bar{p}$ experiments: FENICE[6], DM2[5], DM1[4], BES[8], CLEO[9], NU[10], PS170[11], E835[13], E760[12]: (a) for the mass interval from $p\bar{p}$ threshold to $3.01 \text{ GeV}/c^2$, and (b) for $p\bar{p}$ masses from 2.58 to $4.50 \text{ GeV}/c^2$.

radiative corrections (1%). A comparison of this result with the available e^+e^- data is shown in Fig. 15, and the behavior in the near-threshold region is shown in Fig. 16.

The $e^+e^- \rightarrow p\bar{p}$ cross section is a function of two form factors, but due to the poor determination of the $|G_E/G_M|$ ratio, they cannot be extracted from the data simultaneously with reasonable accuracy. Therefore, the effective form factor $F_p(M_{p\bar{p}})$ is introduced (Eq. (4)), which is proportional to the square root of the measured cross section. This definition of the effective form factor permits comparison of our measurement with measurements from other experiments, most of which were made under the assumption $|G_E| = |G_M|$. The calculated effective form factor is shown in Fig. 17 (linear scale) and Fig. 18 (logarithmic scale), while numerical values are listed in Table VI. These form factor values are obtained as averages over mass-interval width. The four measurements from PS170 [11] with lowest mass are located within the first mass interval of Table VI. Consequently, for the mass region near threshold, where the results from PS170 indicate that the form factor changes rapidly with mass, we calculate the cross section and effective form factor using a smaller mass-interval size. These results are listed in Table VII, and shown in Fig. 19. From Figs. 17, 18, and 19, it is evident that the *BABAR* effective

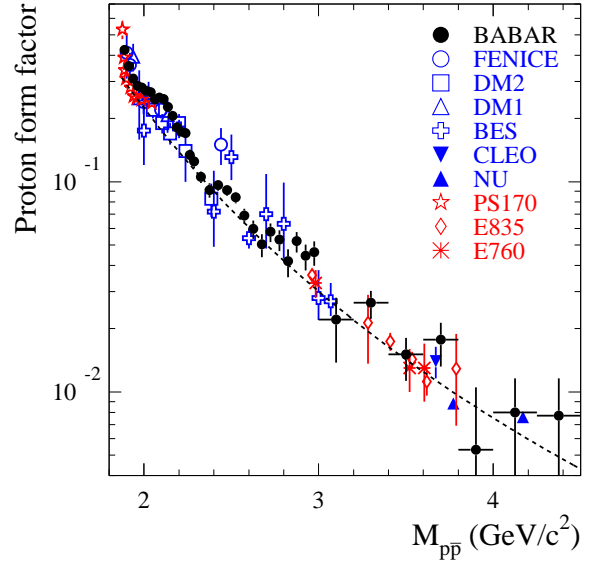


FIG. 18: The proton effective form factor measured in this analysis, in other e^+e^- experiments, and in $p\bar{p}$ experiments, shown on a logarithmic scale: FENICE[6], DM2[5], DM1[4], BES[8], CLEO[9], NU[10], PS170[11], E835[13], E760[12]. The curve corresponds to the QCD-motivated fit described in the text.

form factor results are in reasonable agreement with, and in general more precise than, those from previous experiments. However, in the region $1.88\text{--}2.15 \text{ GeV}/c^2$, the *BABAR* results are systematically above those from the other experiments.

The form factor has a complex mass dependence. The significant increase in the form factor as the $p\bar{p}$ threshold is approached may be due to final-state interaction between the proton and antiproton [29–32]. The rapid decreases of the form factor and cross section near $2.2 \text{ GeV}/c^2$, $2.55 \text{ GeV}/c^2$, and $3 \text{ GeV}/c^2$ have not been discussed in the literature. The form-factor mass dependence below $3 \text{ GeV}/c^2$ is not described satisfactorily by existing models (see, for example, Refs. [33–36]). The dashed curve in Fig. 18 corresponds to a fit of the asymptotic QCD dependence of the proton form factor [37], $F_{p\bar{p}} \sim \alpha_s^2(M_{p\bar{p}}^2)/M_{p\bar{p}}^4 \sim D/(M_{p\bar{p}}^4 \log^2(M_{p\bar{p}}^2/\Lambda^2))$, to the existing data with $M_{p\bar{p}} > 3 \text{ GeV}/c^2$. Here $\Lambda = 0.3 \text{ GeV}$ and D is a free fit parameter. All the data above $3 \text{ GeV}/c^2$ except the two points from Ref. [10] marked “NU” are well described by this function. Adding the points from Ref. [10] changes the fit χ^2/ν from $9/16$ to $41/18$, where ν is the number of degrees of freedom. The measurement of Ref. [10] indicates that the form factor at $M_{p\bar{p}} \approx 4 \text{ GeV}/c^2$ decreases more slowly than predicted by QCD.

TABLE VII: The $p\bar{p}$ invariant-mass interval ($M_{p\bar{p}}$), number of selected events (N) after background subtraction and mass migration, measured cross section ($\sigma_{p\bar{p}}$), and effective form factor for $e^+e^- \rightarrow p\bar{p}$ ($|F_p|$). The quoted errors on N and $\sigma_{p\bar{p}}$ are statistical and systematic, respectively. For the effective form factor, the combined error is listed.

$M_{p\bar{p}}$ (GeV/ c^2)	N	$\sigma_{p\bar{p}}$ (pb)	$ F_p $
1.8765–1.8800	$37 \pm 7 \pm 1$	$534 \pm 94 \pm 39$	0.515 ± 0.050
1.8800–1.8850	$80 \pm 10 \pm 1$	$826 \pm 106 \pm 42$	0.497 ± 0.034
1.8850–1.8900	$67 \pm 10 \pm 1$	$705 \pm 105 \pm 33$	0.403 ± 0.032
1.8900–1.8950	$79 \pm 11 \pm 1$	$886 \pm 121 \pm 41$	0.416 ± 0.030
1.8950–1.9000	$86 \pm 12 \pm 1$	$938 \pm 128 \pm 42$	0.404 ± 0.029
1.9000–1.9050	$70 \pm 11 \pm 1$	$785 \pm 123 \pm 35$	0.353 ± 0.029
1.9050–1.9100	$80 \pm 11 \pm 1$	$937 \pm 135 \pm 41$	0.372 ± 0.028
1.9100–1.9150	$98 \pm 13 \pm 1$	$1096 \pm 142 \pm 46$	0.390 ± 0.027
1.9150–1.9250	$156 \pm 15 \pm 2$	$862 \pm 84 \pm 32$	0.333 ± 0.017
1.9250–1.9375	$188 \pm 16 \pm 3$	$811 \pm 69 \pm 31$	0.309 ± 0.014
1.9375–1.9500	$208 \pm 17 \pm 3$	$887 \pm 72 \pm 33$	0.311 ± 0.014
1.9500–1.9625	$181 \pm 16 \pm 3$	$780 \pm 70 \pm 30$	0.283 ± 0.014
1.9625–1.9750	$209 \pm 17 \pm 3$	$850 \pm 70 \pm 32$	0.288 ± 0.013

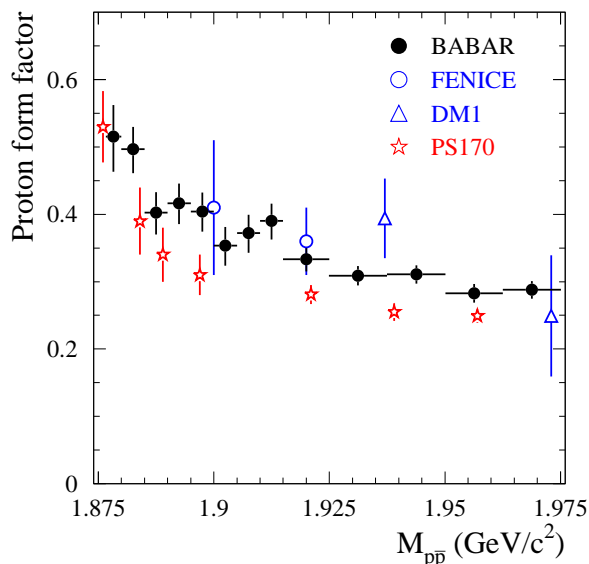


FIG. 19: The proton effective form factor near $p\bar{p}$ threshold measured in this work and in other e^+e^- and $p\bar{p}$ experiments: FENICE[6], DM1[4], PS170[11].

VIII. THE J/ψ AND $\psi(2S)$ DECAYS TO $p\bar{p}$

The differential cross section for ISR production of a narrow resonance (vector meson V), such as J/ψ , decaying into the final state f can be calculated using [38]

$$\frac{d\sigma(s, \theta_\gamma^*)}{d\cos\theta_\gamma^*} = \frac{12\pi^2\Gamma(V \rightarrow e^+e^-)\mathcal{B}(V \rightarrow f)}{m_V s} W(s, x_V, \theta_\gamma^*), \quad (13)$$

where m_V and $\Gamma(V \rightarrow e^+e^-)$ are the mass and electronic width of the vector meson V , $x_V = 1 - m_V^2/s$, and $\mathcal{B}(V \rightarrow f)$ is the branching fraction of V into the final state f . Therefore, the measurement of the num-

ber of $J/\psi \rightarrow p\bar{p}$ decays in $e^+e^- \rightarrow p\bar{p}\gamma$ determines the product of the electronic width and the branching fraction: $\Gamma(J/\psi \rightarrow e^+e^-)\mathcal{B}(J/\psi \rightarrow p\bar{p})$. The $p\bar{p}$ mass spectra for selected events in the J/ψ and $\psi(2S)$ mass regions are shown in Fig. 20. To determine the number of resonance events, each spectrum is fit with a sum of the probability density function (PDF) for signal plus a linear background term. The resonance PDF is a Breit-Wigner function convolved with a double-Gaussian function describing detector resolution. The Breit-Wigner widths and masses for the J/ψ and $\psi(2S)$ resonances are fixed at their nominal values [39]. The parameters of the resolution function are determined from simulation. To account for possible differences in detector response between data and simulation, the simulated resolution function is modified by adding in quadrature an additional σ_G to both the standard-deviation values of the double-Gaussian function, and introducing a shift of the central value of the resonance mass. The free parameters in the fit to the J/ψ mass region are the number of resonance events, the total number of nonresonant background events, the slope of the background, σ_G , and the mass shift. In the $\psi(2S)$ fit the σ_G and mass shift values are fixed to those obtained for the J/ψ .

The fit results are shown as the curves in Fig. 20. We find $N_{J/\psi} = 821 \pm 30$ and $N_{\psi(2S)} = 43.5 \pm 7.7$; the number of nonresonant events is 62 ± 11 for the 3–3.2 GeV/ c^2 mass interval, and 19 ± 6 for the 3.6–3.8 GeV/ c^2 interval. These values are used to extract the nonresonant $e^+e^- \rightarrow p\bar{p}$ cross section. Since the background subtraction procedure for nonresonant events (see Sec. IV D) uses events with $30 < \chi_p^2 < 60$, the mass spectra obtained with this requirement must also be fit. The numbers of J/ψ and nonresonant events are found to be 40 ± 8 and 19 ± 7 . The ratio of J/ψ events with $30 < \chi_p^2 < 60$ to the number with $\chi_p^2 < 30$, 0.049 ± 0.010 , is in good agreement with the value of $\beta_{p\bar{p}\gamma} = 0.049 \pm 0.001$ obtained from simulation. In the $\psi(2S)$ mass region, no

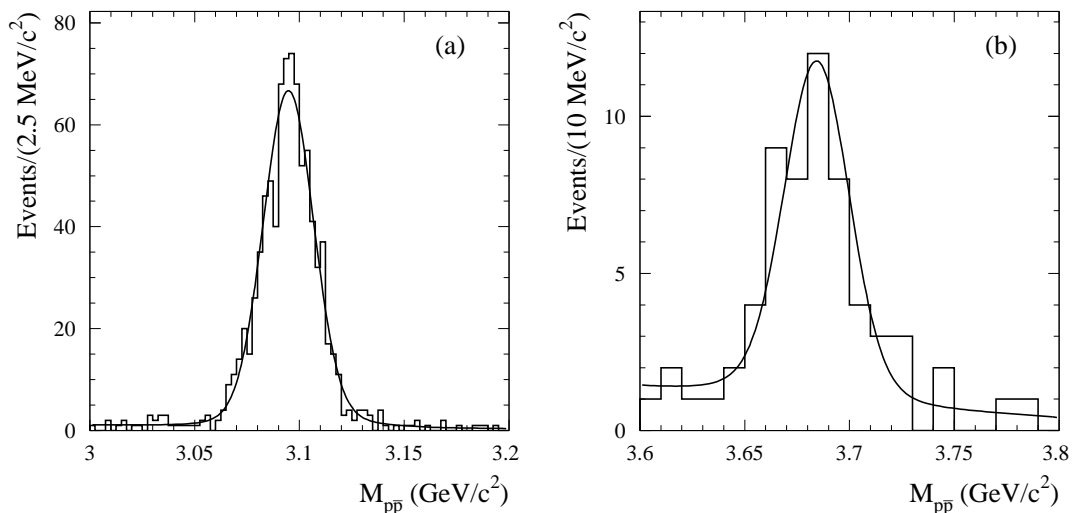


FIG. 20: The $p\bar{p}$ mass spectrum in the mass region (a) near the J/ψ , and (b) near the $\psi(2S)$. The curves display the results of the fits described in the text.

events are found with $30 < \chi_p^2 < 60$. The remaining fit parameters are $\sigma_G = 5.0 \pm 1.0 \text{ MeV}/c^2$ and $M_{J/\psi} - M_{J/\psi}^{MC} = -(1.7 \pm 0.5) \text{ MeV}/c^2$. The fitted value of σ_G leads to an increase in simulation resolution (11 MeV/c^2) of 10%.

The corresponding detection efficiency values are estimated from MC simulation. The event generator uses experimental information to describe the the angular distribution of protons in J/ψ and $\psi(2S)$ decay to $p\bar{p}$. Specifically, each distribution is described by the dependence $1 + a \cos^2 \theta_p$, with $a = 0.672 \pm 0.034$ for J/ψ decay [40, 41] and $a = 0.72 \pm 0.13$ for $\psi(2S)$ decay [42, 43]. The model error in the detection efficiency due to the uncertainty of a is negligible. The efficiencies are found to be $\varepsilon_{MC} = 0.174 \pm 0.001$ for J/ψ and $\varepsilon_{MC} = 0.172 \pm 0.001$ for $\psi(2S)$. The fractional correction for the data-MC simulation differences discussed in Sec. VI is $-(3.6 \pm 2.2)\%$.

The cross section for $e^+e^- \rightarrow \psi\gamma \rightarrow p\bar{p}\gamma$ for $20^\circ < \theta_\gamma^* < 160^\circ$ is calculated as

$$\sigma(20^\circ < \theta_\gamma^* < 160^\circ) = \frac{N_\psi}{\varepsilon R L}, \quad (14)$$

yielding $(10.4 \pm 0.4 \pm 0.3) \text{ fb}$ and $(0.55 \pm 0.10 \pm 0.02) \text{ fb}$ for the J/ψ and $\psi(2S)$ states, respectively. The radiative-correction factor $R = \sigma/\sigma_{Born}$ is 1.007 ± 0.010 for the J/ψ and 1.011 ± 0.010 for the $\psi(2S)$, where both values are obtained from MC simulation at the generator level.

The total integrated luminosity for the data sample is $(469 \pm 5) \text{ fb}^{-1}$. From the measured cross sections and Eq. (13), the following products are determined:

$$\begin{aligned} \Gamma(J/\psi \rightarrow e^+e^-) \mathcal{B}(J/\psi \rightarrow p\bar{p}) &= \\ & (11.3 \pm 0.4 \pm 0.3) \text{ eV}, \\ \Gamma(\psi(2S) \rightarrow e^+e^-) \mathcal{B}(\psi(2S) \rightarrow p\bar{p}) &= \\ & (0.67 \pm 0.12 \pm 0.02) \text{ eV}. \end{aligned} \quad (15)$$

The systematic errors include the uncertainties on the detection efficiencies, the integrated luminosity, and the radiative corrections.

Using the nominal values for the electronic widths [39], we obtain the branching fractions

$$\begin{aligned} \mathcal{B}(J/\psi \rightarrow p\bar{p}) &= (2.04 \pm 0.07 \pm 0.07) \times 10^{-3}, \\ \mathcal{B}(\psi(2S) \rightarrow p\bar{p}) &= (2.86 \pm 0.51 \pm 0.09) \times 10^{-4}. \end{aligned} \quad (16)$$

These values are in agreement with the nominal values [39] of $(2.17 \pm 0.07) \times 10^{-3}$ and $(2.76 \pm 0.12) \times 10^{-4}$, respectively, and with the recent high-precision BESIII result [44] $\mathcal{B}(J/\psi \rightarrow p\bar{p}) = (2.112 \pm 0.004 \pm 0.031) \times 10^{-3}$.

IX. SUMMARY

The process $e^+e^- \rightarrow p\bar{p}\gamma$ has been studied for $p\bar{p}$ invariant masses up to $4.5 \text{ GeV}/c^2$. From the measured $p\bar{p}$ mass spectrum we extract the $e^+e^- \rightarrow p\bar{p}$ cross section and the proton effective form factor. The form factor has a complex mass dependence. The near-threshold enhancement of the form factor observed in the PS170 experiment [11] is confirmed in this study. There are also three mass regions, near $2.2 \text{ GeV}/c^2$, $2.55 \text{ GeV}/c^2$, and $3 \text{ GeV}/c^2$, that exhibit step decreases in the form factor and cross section.

By analysing the proton angular distributions we measure the mass dependence of the ratio $|G_E/G_M|$ for $M_{p\bar{p}}$ from threshold to $3 \text{ GeV}/c^2$. For masses up to $2.1 \text{ GeV}/c^2$, this ratio is found to be significantly greater than unity, in disagreement with the PS170 measurement [11]. The asymmetry in the proton angular distribution is found to be

$$A_{\cos \theta_p} = -0.025 \pm 0.014 \pm 0.003$$

for $M_{p\bar{p}} < 3 \text{ GeV}/c^2$.

From the measured event yields for $e^+e^- \rightarrow J/\psi\gamma \rightarrow p\bar{p}\gamma$ and $e^+e^- \rightarrow \psi(2S)\gamma \rightarrow p\bar{p}\gamma$, we determine the branching fraction values

$$\begin{aligned}\mathcal{B}(J/\psi \rightarrow p\bar{p}) &= (2.04 \pm 0.07 \pm 0.07) \times 10^{-3}, \\ \mathcal{B}(\psi(2S) \rightarrow p\bar{p}) &= (2.86 \pm 0.51 \pm 0.09) \times 10^{-4}.\end{aligned}$$

Our results on the cross section, form factors, and J/ψ and $\psi(2S)$ decays agree with, and supersede, earlier *BABAR* measurements [14].

X. ACKNOWLEDGMENTS

We are grateful for the extraordinary contributions of our PEP-II colleagues in achieving the excellent luminosity and machine conditions that have made this work possible. The success of this project also relies critically on

the expertise and dedication of the computing organizations that support *BABAR*. The collaborating institutions wish to thank SLAC for its support and the kind hospitality extended to them. This work is supported by the US Department of Energy and National Science Foundation, the Natural Sciences and Engineering Research Council (Canada), the Commissariat à l'Énergie Atomique and Institut National de Physique Nucléaire et de Physique des Particules (France), the Bundesministerium für Bildung und Forschung and Deutsche Forschungsgemeinschaft (Germany), the Istituto Nazionale di Fisica Nucleare (Italy), the Foundation for Fundamental Research on Matter (The Netherlands), the Research Council of Norway, the Ministry of Education and Science of the Russian Federation, Ministerio de Ciencia e Innovación (Spain), and the Science and Technology Facilities Council (United Kingdom). Individuals have received support from the Marie-Curie IEF program (European Union) and the A. P. Sloan Foundation (USA).

-
- [1] G. Bonneau and F. Martin, Nucl. Phys. B **27**, 381 (1971).
 [2] A. B. Arbuzov and T. V. Kopylova, JHEP **1204**, 009 (2012).
 [3] H. Czyz *et al.*, Eur. Phys. J. C **35**, 527 (2004).
 [4] B. Delcourt *et al.* (DM1 Collaboration), Phys. Lett. B **86**, 395 (1979).
 [5] D. Bisello *et al.* (DM2 Collaboration), Nucl. Phys. B **224**, 379 (1983); Z. Phys. C **48**, 23 (1990).
 [6] A. Antonelli *et al.* (FENICE Collaboration), Nucl. Phys. B **517**, 3 (1998).
 [7] M. Castellano *et al.*, Nuovo Cim. A **14**, 1 (1973).
 [8] M. Ablikim *et al.* (BES Collaboration), Phys. Lett. B **630**, 14 (2005).
 [9] T. K. Pedlar *et al.* (CLEO Collaboration), Phys. Rev. Lett. **95**, 261803 (2005).
 [10] K. K. Seth, S. Dobbs, Z. Metreveli, A. Tomaradze, T. Xiao and G. Bonvicini, arXiv:1210.1596 [hep-ex].
 [11] G. Bardin *et al.* (PS170 Collaboration), Nucl. Phys. B **411**, 3 (1994).
 [12] T. A. Armstrong *et al.* (E760 Collaboration), Phys. Rev. Lett. **70**, 1212 (1993).
 [13] M. Ambrogiani *et al.* (E835 Collaboration), Phys. Rev. D **60**, 032002 (1999); M. Andreotti *et al.*, Phys. Lett. B **559**, 20 (2003).
 [14] B. Aubert *et al.* (*BABAR* Collaboration), Phys. Rev. D **73**, 012005 (2006).
 [15] B. Aubert *et al.* (*BABAR* Collaboration), Nucl. Instr. and Meth. A **479**, 1 (2002).
 [16] W. Menges, IEEE Nucl. Sci. Symp. Conf. Rec. **5**, 1470 (2006).
 [17] H. Czyz and J. H. Kühn, Eur. Phys. J. C **18**, 497 (2001).
 [18] M. Caffo, H. Czyz, and E. Remiddi, Nuovo Cim. A **110**, 515 (1997); Phys. Lett. B **327**, 369 (1994).
 [19] E. Barberio and Z. Was, Comput. Phys. Commun. **79**, 291 (1994).
 [20] T. Sjöstrand, Comput. Phys. Commun. **82**, 74 (1994).
 [21] S. Agostinelli *et al.*, Nucl. Instr. and Meth. A **506**, 250 (2003).
 [22] V. L. Chernyak, private communication.
 [23] P. G. Blunden, W. Melnitchouk and J. A. Tjion, Phys. Rev. Lett. **91**, 142304 (2003).
 [24] J. Arrington, Phys. Rev. C **69**, 022201 (2004).
 [25] O. Gayou *et al.*, Phys. Rev. Lett. **88**, 092301 (2002).
 [26] V. Punjabi *et al.*, Phys. Rev. C **71**, 055202 (2005); erratum-ibid. C **71**, 069902 (2005).
 [27] A. J. R. Puckett *et al.*, Phys. Rev. Lett. **104**, 242301 (2010).
 [28] E. Tomasi-Gustafsson *et al.*, Phys. Lett. B **659**, 197 (2008).
 [29] J. Haidenbauer *et al.*, Phys. Lett. B **643**, 29 (2006).
 [30] G. Y. Chen, H. R. Dong and J. P. Ma, Phys. Lett. B **692**, 136 (2010).
 [31] V. F. Dmitriev and A. I. Milstein, Nucl. Phys. Proc. Suppl. **181-182**, 66 (2008).
 [32] O. D. Dalkarov, P. A. Khakhulin and A. Y. Voronin, Nucl. Phys. A **833**, 104 (2010).
 [33] M. A. Belushkin, H.-W. Hammer and U.-G. Meissner, Phys. Rev. C **75**, 035202 (2007).
 [34] J. P. B. C. de Melo *et al.*, Phys. Lett. B **671**, 153 (2009).
 [35] S. Furuichi, H. Ishikawa and K. Watanabe, Phys. Rev. C **81**, 045209 (2010).
 [36] E. L. Lomon and S. Pacetti, Phys. Rev. D **85**, 113004 (2012); erratum-ibid. D **86**, 039901 (2012).
 [37] V. L. Chernyak, A. R. Zhitnitsky, JETP Lett. **25**, 510 (1977); G. Lepage, S. Brodsky, Phys. Rev. Lett. **43**, 545 (1979).
 [38] M. Benayoun *et al.*, Mod. Phys. Lett. A **14**, 2605 (1999).
 [39] J. Beringer *et al.* (Particle Data Group), Phys. Rev. D **86**, 010001 (2012).
 [40] D. Pallin *et al.* (DM2 Collaboration), Nucl. Phys. B **292**, 653 (1987); R. Brandelik *et al.* (DASP Collaboration), Z. Phys. C **1**, 233 (1976); I. Peruzzi *et al.* (MARK I Collaboration), Phys. Rev. D **17**, 2901 (1978); M. W. Eaton *et al.* (MARK II Collaboration), Phys. Rev. D **29**, 804 (1984).
 [41] J. Z. Bai *et al.* (BES Collaboration), Phys. Lett. B **591**, 42 (2004).
 [42] M. Ambrogiani *et al.* (E835 Collaboration), Phys. Lett.

- B **610**, 177 (2005).
- [43] M. Ablikim *et al.* (BES Collaboration), Phys. Lett. B **648**, 149 (2007).
- [44] M. Ablikim *et al.* (BESIII Collaboration), Phys. Rev. D **86**, 032014 (2012).